Genesis and evolution of the lithospheric mantle beneath the Buffalo Head Terrane, Alberta (Canada)[☆]

S. Aulbach[a,*], W.L. Griffin[a,b], S.Y. O'Reilly[a], Tom E. McCandless[c]

[a] GEMOC ARC National Key Centre, Macquarie University, Australia
[b] CSIRO Exploration and Mining, North Ryde, Australia
[c] Ashton Mining Canada Inc., North Vancouver, Canada

Abstract

Mantle xenoliths and xenocrysts were retrieved from three of the 88–86 Ma Buffalo Hills kimberlites (K6, K11, K14) for a reconnaissance study of the subcontinental lithospheric mantle (SCLM) beneath the Buffalo Head Terrane (Alberta, Canada). The xenoliths include spinel lherzolites, one garnet spinel lherzolite, garnet harzburgites, one sheared garnet lherzolite and pyroxenites. Pyroxenitic and wehrlitic garnet xenocrysts are derived primarily from the shallow mantle and lherzolitic garnet xenocrysts from the deep mantle. Harzburgite with Ca-saturated garnets is concentrated in a layer between ∼ 135–165 km depth. Garnet xenocrysts define a model conductive paleogeotherm corresponding to a heat flow of 38–39 mW/m². The sheared garnet lherzolite lies on an inflection of this geotherm and may constrain the depth of the lithosphere–asthenosphere boundary (LAB) beneath this region to ca 180 km depth.

A loss of >20% partial melt is recorded by spinel lherzolites and up to 60% by the garnet harzburgites, which may be related to lithosphere formation. The mantle was subsequently modified during at least two metasomatic events. An older metasomatic event is evident in incompatible-element enrichments in homogeneous equilibrated garnet and clinopyroxene. Silicate melt metasomatism predominated in the deep lithosphere and led to enrichments in the HFSE with minor enrichments in LREE. Metasomatism by small-volume volatile-rich melts, such as carbonatite, appears to have been more important in the shallow lithosphere and led to enrichments in LREE with minor enrichments in HFSE. An intermediate metasomatic style, possibly a signature of volatile-rich silicate melts, is also recognised. These metasomatic styles may be related through modification of a single melt during progressive interaction with the mantle. This metasomatism is suggested to have occurred during Paleoproterozoic rifting of the Buffalo Head Terrane from the neighbouring Rae Province and may be responsible for the evolution of some samples toward unradiogenic Nd and Hf isotopic compositions.

Disturbed Re–Os isotope systematics, evident in implausible model ages, were obtained in situ for sulfides in several spinel lherzolites and suggest that many sulfides are secondary (metasomatic) or mixtures of primary and secondary sulfides. Sulfide in one peridotite has unradiogenic $^{187}Os/^{188}Os$ and gives a model age of 1.89 ± 0.38 Ga. This age coincides with the inferred emplacement of mafic sheets in the crust and suggests that the melts parental to the intrusions interacted with the lithospheric mantle.

A younger metasomatic event is indicated by the occurrence of sulfide-rich melt patches, unequilibrated mineral compositions and overgrowths on spinel that are Ti-, Cr- and Fe-rich but Zn-poor. Subsequent cooling is recorded by fine exsolution lamellae in the pyroxenes and by arrested mineral reactions.

If the lithosphere beneath the Buffalo Head Terrane was formed in the Archaean, any unambiguous signatures of this ancient origin may have been obliterated during these multiple events.

1. Introduction

In areas with thick sedimentary cover and recent glacial deposits, such as the Buffalo Head Terrane (hereafter, BHT) in northern Alberta, information on the nature of the crust and mantle is often restricted to remote sensing and drill cores. Using these methods, a new kimberlite province, erupted at 88–86 Ma (Buffalo Hills kimberlites), was identified in the centre of the BHT (Carlson et al., 1999). This discovery has provided an opportunity to directly study the lithosphere beneath the BHT by means of mantle samples transported to the surface. Xenoliths and xenocrysts were retrieved from three kimberlites (K6, K11, K14) for a reconnaissance geochemical study (major-element, trace-element and isotopic) in order to constrain the paleogeotherm and the stratigraphy of the subcontinental lithospheric mantle (SCLM) beneath this region, and to assess its origin and evolution. In a parallel study, xenocryst minerals from 29 of the 37 known kimberlite bodies from Buffalo Hills have been investigated at the province scale (Hood and McCandless, 2003). Preliminary results indicate that there are regional variations in distribution and composition of the xenocrysts. Furthermore, kimberlites in the southern part of the province have higher abundances of metasomatic minerals and are dominated by a lower-Cr assemblage, which may be directly related to their lower diamond grade (Hood and McCandless, 2003).

Geophysics and crustal geology of the area provide important constraints on any interpretation of data from the SCLM, as major tectonothermal events in the crust are expressions of mantle processes. A prolonged episode of rifting, subduction beneath the BHT, emplacement of mafic sheets and kimberlite magmatism are some of the events recognised in the crust that may entail reworking of the underlying SCLM. Ross and Eaton (2002) suggest that the BHT represents a collage of Paleoproterozoic crust formed on an Archaean microcontinent that has been extensively modified during Proterozoic magmatism. This study is designed to investigate whether and how these events have affected the SCLM beneath the BHT, and whether any Archaean signatures have survived the postulated Proterozoic reworking. Furthermore, comparisons will be made with peridotite suites from the Slave craton to the north, in order to establish whether any relationship exists between these mantle sections, given their present-day proximity.

2. Geology

The Paleoproterozoic BHT is part of the western Canadian Shield in northern Alberta. Because of its Phanerozoic rock cover, the boundaries of the BHT and other covered domains have been defined based on aeromagnetic data, using the overall signature, internal fabric and contrasts with adjacent domains (Ross, 2000), and geochronology on drill core recovered during petroleum exploration (Thériault and Ross, 1991). The BHT is truncated to the south by the Snowbird Tectonic Zone, whereas to the north, it is attenuated with the Great Slave Lake Shear Zone (Fig. 1). In the east, the BHT is separated from the Rae Province by the younger (1.987 to 1.900 Ga) Taltson magmatic zone. In the west, it is separated from the Nova Terrane by the magmatic rocks of the Ksituan High (Ross et al., 1991; Ross and Eaton, 1997; Carlson et al., 1999). The BHT is transected in the south by the Peace River Arch, a lineament where elevated heat flow and anomalous crustal uplift have been observed and which has been active since the Proterozoic (Carlson et al., 1999).

The tectonic setting of the BHT is not well constrained because its lithosphere has been overprinted by younger events (Ross, 2002). Archaean inheritance ages were obtained for Proterozoic basement rocks of
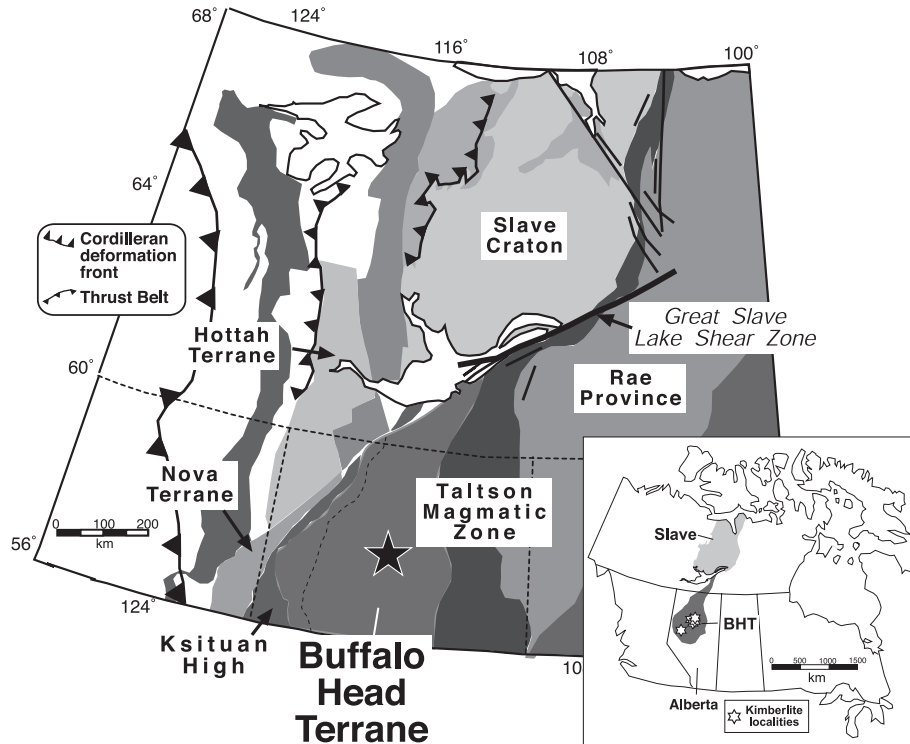
Fig. 1. Domain map showing the BHT and neighbouring structural elements (after Hoffman, 1989). Star shows sample locality. Inset shows map of western Canada with outlines of BHT and Slave craton.

the BHT by Villeneuve et al. (quoted in Ross and Eaton, 1997), suggesting an older component is present. The similarity of basement ages (2.4–2.1 Ga) and Nd isotope systematics for the BHT and the adjacent Rae Province suggests that they formed a single crustal domain by 2.4 Ga (McNicoll et al., 2000). The occurrence of 2.34 Ga mafic to ultramafic rocks in the contact area between the BHT and the Rae Province may indicate that these two entities were separating by that time (Ross et al., 1991; Bostock and van Breemen, 1994). Rifting was followed by subduction at the eastern and western terrane margin, with the subduction polarity facing away from the BHT. This resulted in coeval arc magmatism that produced the 1980–1920 Ma Taltson magmatic zone and the 1986–1900 Ma Ksituan High (Ross et al., 1991; Bostock and van Breemen, 1994).

Postcollisional underplating of mafic rocks in the core of the BHT may be manifested by the 1.89 to 1.76 Ga sheet-like mafic sills of the Winagami reflection sequence, a package of reflectors in the upper

crust of the Peace River Arch region, (Ross and Eaton, 1997, and references therein). The high-grade metamorphic Buffalo Head Terrane was eventually covered by up to 1600 m of Devonian and Cretaceous sediments (Carlson et al., 1999). Between 88 and 86 Ma, the centre of the BHT was intruded by the kimberlites of the Buffalo Hills kimberlite province (Carlson et al., 1999; Ross et al., 2000).

3. Petrography

Thirty-one xenoliths were retrieved from three different kimberlites (K6, K11, K14) for this study. Two major xenolith types are present: peridotites and pyroxenites. Our study includes 22 peridotites and nine pyroxenites. Fig. 2 shows examples of the rock types sampled by the kimberlites. Petrographic details are given in Table 1.

Peridotites encompass four mineralogical varieties: 15 spinel peridotites, one garnet spinel lherzolite
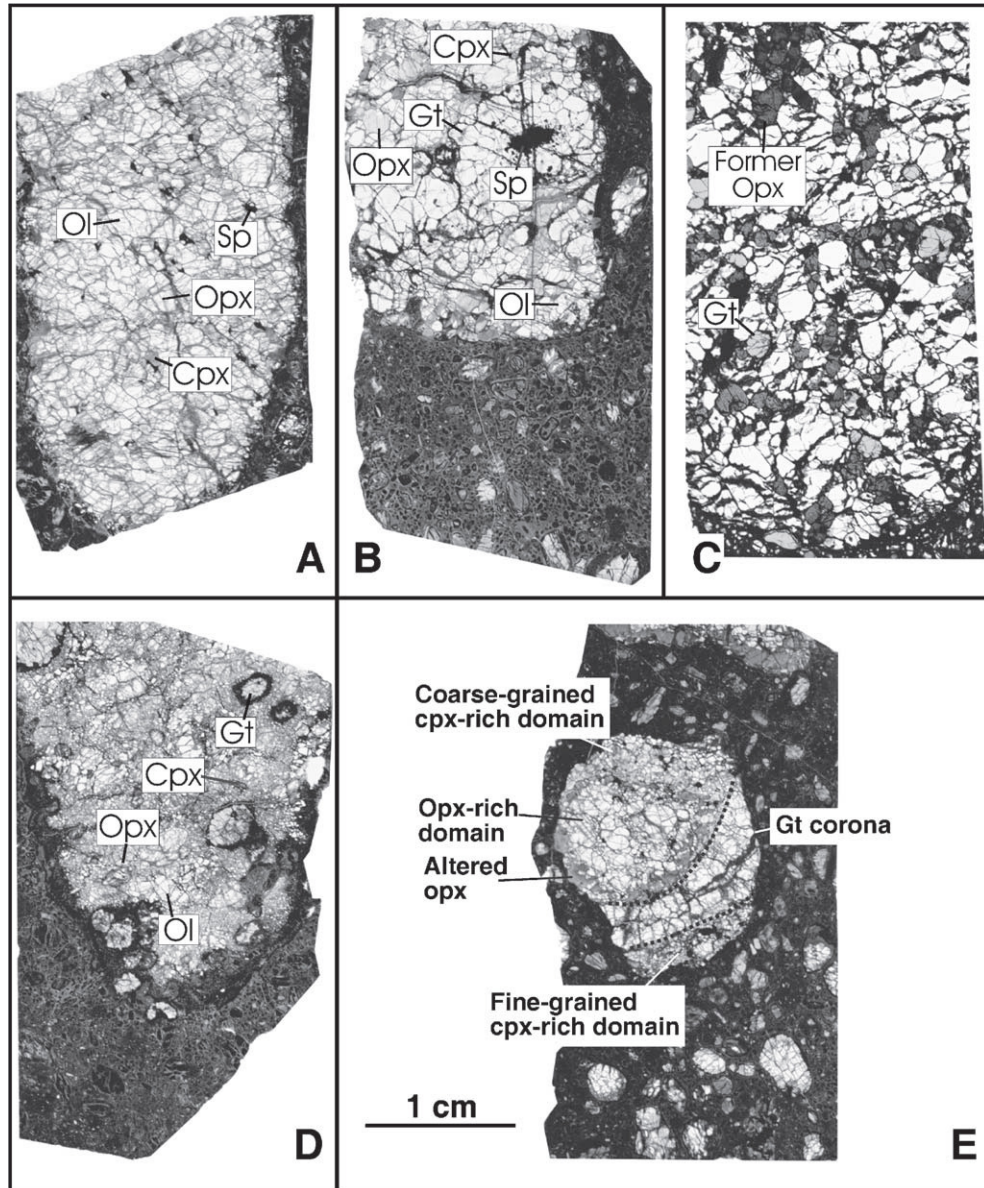
Fig. 2. Xenoliths from the Buffalo Hills kimberlites in thin section (plane-polarised light). Some minerals are indicated (ol: olivine, sp: spinel, opx: orthopyroxene, cpx: clinopyroxene, gt: garnet). (A) Spinel lherzolite; (B) garnet spinel lherzolite showing spinel blebs in large garnet clusters; (C) garnet harzburgite with altered opx; (D) sheared garnet lherzolite; (E) corona-structured garnet pyroxenite; garnet-free pyroxenite is visible at top of section. The scale is the same for all sections as indicated in (E).

(K14-3a), three garnet peridotites (with altered pyroxene; all from kimberlite K11) and one sheared garnet lherzolite (K14-1). Most spinel lherzolites are medium-grained rocks with equant to tabular, foliated microstructure (Fig. 2A). Spinel peridotites have ol-

ivine modes ranging from 56% to 87%, orthopyroxene modes from 10% to 38% and clinopyroxene modes from 1% to 10%. The garnet spinel lherzolite has a medium-grained equant microstructure with large garnet clusters that contain numerous inclusions

Table 1
Petrographic details

Sample #	Rock type	Size [cm]	Microstructure	Assemblage	Modes
K6-1	sp lherz	5	medium-eq/tab fol	ol,opx,cpx,sp,sf	87,11,1,1,<1
K6-2a	sp lherz	2.5	medium-eq	ol,opx,cpx,sp,sf	84,10,5,1,<1
K6-2b	sp lherz	5	medium-eq/tab fol	ol,opx,cpx,sp	na
K6-2b2	gt pyrox	0.3	fine-eq	gt,opx	na
K6-3	sp lherz	5	coarse-eq/tab fol	ol,opx,cpx,sp	75,23,1,1
K6-4	sp lherz	5	medium-eq/tab fol	ol,opx,cpx,sp	70,26,4,<1
K6-5a	sp-lherz	2.5	medium-eq/tab fol	ol,opx,cpx,sp	na
K6-5b	pyrox	2	fine-mosaic	opx,cpx,sf	89,10,1
K11-3	gt perid	5	coarse-tab fol	ol,alt opx,gt,sp	85,14,1,<1
K11-5	gt perid	5	coarse-eq/tab fol	ol,alt opx,gt	78,19,3
K11-6	gt perid	3	coarse-tab	ol,alt opx,gt	80,19,1
K14-1	gt lherz	4	porph-tab	ol,opx,cpx,gt	78,11,2,9
K14-2a	gt pyrox	2	mosaic-porph	gt,cpx,opx,rut,sf	8,35,57,<1,<1
K14-2ba	sp lherz	4	medium-tab fol	ol,opx,cpx,sp,sf	81,15,2,2,<1
K14-2bb	gt pyrox	2	mosaic-porph	gt,cpx,opx,sf	4,53,43,<1
K14-2c	sp lherz	2	coarse-tab	ol,opx,cpx,sp	59,38,2,1
K14-3a	gt sp lherz	2.5	medium-eq/tab fol	ol,opx,cpx,gt,sp,ilm,sf	43,11,2,42,2,<1
K14-3b2	perid	0.4	?porph	ol,cpx,sf	na
K14-3c	gt pyrox	2	medium-eq	gt,cpx,alt opx,rut,sf	4,49,47,<1,<1
K14-4a	sp lherz	5	coarse-tab grano	ol,opx,cpx,sp	72,16,10,2
K14-4b	gt pyrox	1.5	medium-eq	gt,cpx	na
K14-5a	sp harz	1	medium-eq/tab grano	ol,opx,sp	56,44,<1
K14-5b	sp lherz	2.5	coarse-eq/tab fol	ol,opx,cpx,sp,sf	75,18,5,2,<1
K14-5c	gt pyrox	2	corona	gt,cpx,opx,sf	na
K14-5c2	pyrox	2	mosaic-porph	cpx,opx	na
K14-5d	sp lherz	1.5	medium-eq/tab grano	ol,opx,cpx,sp,sf	67,28,2,3,<1
K14-5f	gt pyrox	2.5	mosaic-porph	gt,cpx,opx,sf	7,21,72,<1
K14-5g	harz	1	na	ol,opx	85,15
K14-6	sp lherz	5	medium-eq/tab grano	ol,opx,cpx,sp,sf	80,14,5,1,<1
K14-7a	sp lherz	5	coarse-eq/tab fol	ol,opx,cpx,sp,sf	82,11,7,<1,<1
K14-8	sp lherz	5	coarse-eq/tab grano	ol,opx,cpx,sp	77,21,1,1

Petrographic data: sp: spinel; gt: garnet; lherz: lherzolite; harz: harzburgite; perid: peridotite; pyrox: pyroxenite; eq: equant; tab: tabular; fol: foliated; porph: porphyroclasitc; grano: granoblastic; ol: olivine; opx: orthopyroxene; cpx: clinopyroxene; sf: sulfide; ilm: ilmenite; rut: rutile; alt: altered; na: not available.

of spinel and are arranged around large blebs of spinel (Fig. 2B). Its modal proportions of 43% olivine, 11% orthopyroxene, 2% clinopyroxene, 42% garnet and 2% spinel may not be representative of the actual modes, considering the sample size (2.5 cm) and the size of the garnet clusters (up to 1 cm). The three garnet peridotites are inferred to have been pyroxene-bearing before alteration (Fig. 2C). They have medium- to coarse-grained equant to tabular microstructure, with olivine modes ranging from 78% to 85%, garnet modes 1% to 3% and modes of former pyroxene of 14–19%. The sheared garnet lherzolite has a mosaic–porphyroclastic foliated microstructure (Fig. 2D). Its mineral modes are 78% olivine, 11% orthopyroxene, 2% clinopyroxene and 9% garnet. Some

xenoliths from the Buffalo Hills kimberlites are quite small, and this contributes to uncertainty in the point-counted mode estimates. Jerde et al. (1993) considered the error in estimating modes to be around 10% for medium- to coarse-grained rocks.

Eight of the peridotites contain accessory sulfides, most of which have polyhedral or spherical shapes. Interstitial sulfides are slightly more frequent than enclosed ones, which are hosted by olivine, orthopyroxene and clinopyroxene. Spinel lherzolite K14-5b contains an oval melt patch ca. 0.5 mm in diameter, along with several smaller melt patches. Half of the large melt patch is made up of a cluster of polyhedral sulfide grains, one of which is intergrown with skeletal spinel.

Xenoliths of the pyroxenite suite include mostly medium-grained equant or mosaic porphyroclastic (as an analogy to peridotites) varieties. Orthopyroxene modes range from 43% to 89%, clinopyroxene modes from 0% to 53% and garnet modes from 0% to 8%. Six of the pyroxenites contain accessory sulfide and two contain accessory rutile. One sample has a striking corona structure that implies former grain sizes >1 cm (Fig. 2E). It consists of five distinct domains: (1) a broad garnet corona; (2) a domain of large orthopyroxene grains with garnet necklaces, rimmed by (3) a ring of almost completely altered orthopyroxene; (4) a domain of large clinopyroxene grains and garnet strings adjacent to (1) and (3); (5) a domain of small clinopyroxene and garnet grains adjacent to (1). Garnet necklaces around orthopyroxene, suggestive of exsolution processes, occur in several other garnet pyroxenites.

4. Analytical methods

4.1. Electron probe microanalysis (EPMA)

Major-element contents were collected using the CAMECA Camebax SX50 electron microprobe in the GEMOC National Key Centre, Department of Earth and Planetary Sciences, Macquarie University. Silicates were analysed with a 15 kV acceleration voltage and counting times of 10 s on the peak, 5 s on each side of the background. In general, totals between 99% and 101% oxides were accepted; in some cases, they lie between 98.5 and 101.5. Sulfide analyses were performed with an accelerating voltage of 20 kV and a beam current of 20 nA. Counting times were 20 s on the peak and 10 s on each side of the background. The PAP matrix correction procedure (Pouchou and Pichoir, 1984) was applied to the raw data.

4.2. Laser ablation ICPMS

Laser ablation analyses were performed with a custom-built laser-ablation system (designed by S.E. Jackson) or a Merchantek LUV 266 Nd:YAG UV laser system, both linked to an Agilent 7500 ICPMS. The methods followed those described by Norman et al. (1996) and Xu et al. (1999). Raw data were processed on-line using the GLITTER-software (van Achterberg et al., 1999; see www.es.mq.edu.au/GEMOC).

4.3. Solution Sr–Nd–Hf analyses of garnet and clinopyroxene

Hand-picked clinopyroxene and garnet separates were washed in 6 N HCl, and rinsed in Milli-Q water prior to dissolution in concentrated HF and HNO_3. Sample digestion and chemical separation of the elements of interest follow conventional procedures described in the literature (Patchett and Tatsumoto, 1980; Blichert-Toft et al., 1997; Blichert-Toft, 2001). Sr, Nd and Hf aliquots were analysed on a Nu plasma multicollector ICP–MS at Macquarie University, with blanks generally below 1000, 80 and 60 pg, respectively. Repeated measurements of standard materials during the data acquisition (February to July 2003) yielded the following values: $^{87}Sr/^{86}Sr$ of 0.71024 ± 0.00010 (2 S.D.; $n = 51$) for the SRM-987 standard; $^{87}Sr/^{86}Sr$ of 0.70352 ± 0.00004 ($n = 15$) for BHVO-1; $^{143}Nd/^{144}Nd$ of 0.511138 ± 0.000038 ($n = 42$) for the JMC-321 standard, $^{143}Nd/^{144}Nd$ of 0.513003 ± 0.000043 ($n = 10$) for BHVO-1; $^{176}Hf^{177}Hf$ of 0.282163 ± 0.000002 ($n = 20$) for the JMC-475 standard and $^{176}Hf^{177}Hf$ of 0.283128 ± 0.000090 for BHVO-1 ($n = 8$).

4.4. In situ Re–Os isotope analyses of sulfides

Re and Os isotopic ratios were collected with a New Wave Research LUV266 laser microprobe attached to a Nu plasma multicollector ICP–MS at Macquarie University. Typical laser operating conditions are 4–5 Hz frequency, a beam energy of 2–5 mJ/pulse and spot sizes of 60–80 μm. The set-up used for collection of ion beams consisted of eight Faraday cups, using Os as internal isotope standard for mass fractionation correction, or of a combination of eight Faraday cups plus two ion counters (for masses 185 and 187). Drift on the ion counters was corrected for by bracketing sample analyses with analyses of standard PGE-A, a synthetic PGE-doped NiS bead with known Os isotopic composition. The calibration procedures and the corrections applied, as well as reproducibility of standard material are described in detail in Pearson et al. (2002).

5. Major elements

Representative major-element compositions of minerals in xenoliths are shown in Tables 2–9 (online Tables 2–9). Many orthopyroxenes and clinopyroxenes have exsolved complementary pyroxene and/or spinel; some garnets have exsolved rutile. If not indicated otherwise, the compositions discussed here are obtained from exsolution-free areas of the grains; analyses obtained with defo-

cused electron beam (i.e., where exsolved phases are also sampled) are given in Tables 4 and 5.

5.1. Garnet

In the Cr_2O_3 against CaO plot (Sobolev et al., 1973; Gurney, 1984), most garnets (xenocrystic and in xenoliths) plot in the lherzolite field, but several groups may be distinguished (Fig. 3). One group has correlated CaO and Cr_2O_3 and lies entirely in

Table 2
Representative major-element composition of garnet in xenoliths

Sample	K6-2b2	K11-5	K11-5	K11-6	K14-1	K14-2a	K14-3a
n	43	5	21	8	56	14	23
Comment		?primary	?metasomatised	core			
Type	gt pyrox	alt gt harz	alt gt harz	alt gt harz	gt lherz	gt pyrox	gt lherz
SiO_2	40.93	41.29	41.17	42.67	42.01	41.45	41.83
TiO_2	<0.06	0.79	0.11	0.27	0.79	<0.06	<0.06
Al_2O_3	23.01	17.98	17.69	18.91	19.35	23.00	21.70
Cr_2O_3	0.50	6.96	7.59	5.89	3.73	0.35	2.01
FeO^{total}	14.49	7.21	7.21	6.95	8.19	13.44	9.90
MnO	0.47	0.21	0.24	0.21	0.21	0.46	0.51
MgO	15.79	21.72	19.40	20.88	20.81	16.43	18.09
CaO	5.27	4.10	6.50	5.18	4.81	5.16	5.87
NiO	<0.08	<0.08	<0.08	<0.08	<0.08	<0.08	<0.08
Na_2O	<0.04	<0.04	<0.04	<0.04	0.09	<0.04	<0.04
K_2O	<0.04	<0.04	<0.04	<0.04	<0.04	<0.04	<0.04
Total	100.5	100.3	100.0	101.0	100.0	100.4	100.0
Mg#	66.0	84.3	82.7	84.3	81.9	68.6	76.5
Cr#	1.4	20.6	22.3	17.3	11.5	1.0	5.9

Sample	K14-5c (2) max	K14-5c (2) avg	K14-5c (4) min	K14-5c (4) avg	K14-5c (5) max	K14-5c (5) max	K14-5c (5) avg
n		11		9			5
Comment	domain 2	domain 2	domain 4	domain 4	domain 5	domain 5	domain 5
Type	gt pyrox	gt pyrox	gt pyrox	gt pyrox	gt pyrox	gt pyrox	gt pyrox
SiO_2	41.47	41.32	41.32	41.66	42.45	42.22	42.34
TiO_2	<0.06	<0.06	<0.06	<0.06	0.07	<0.06	<0.06
Al_2O_3	23.28	23.08	22.85	23.02	23.43	23.10	23.24
Cr_2O_3	0.23	0.17	<0.09	0.11	0.15	0.10	0.13
FeO^{total}	16.31	15.89	14.62	15.10	13.84	13.41	13.60
MnO	0.36	0.31	0.19	0.22	0.25	0.23	0.24
MgO	15.43	15.07	15.19	15.36	17.23	17.00	17.09
CaO	5.05	4.97	5.25	5.40	4.97	4.69	4.83
NiO	0.10	<0.08	<0.08	<0.08	0.08	<0.08	<0.08
Na_2O	0.05	<0.04	<0.04	<0.04	<0.04	<0.04	<0.04
K_2O	<0.04	<0.04	<0.04	<0.04	<0.04	<0.04	<0.04
Total	101.3	100.9	100.2	100.9	102.2	101.1	101.5
Mg#	63.6	62.8	63.7	64.5	69.4	68.8	69.1
Cr#	0.6	0.5	0.2	0.3	0.4	0.3	0.4

Representative major-element composition of garnet in xenoliths (wt.%); n: number of analyses; Mg# = molar [100 Mg/(Mg + Fe)]; Cr# = molar [100 Cr/(Cr + A1)]; max, min, avg are maximum, minimum and average values for compositionally zoned minerals; domains denote distinct areas in corona-structured sample; xenocr: xenocryst; for other abbreviations, see Table 1.

Table 3
Average major-element composition of garnet xenocrysts

Sample	Avg fertile lherz	Avg depl lherz	Avg sili metas lherz	Avg phlog metas lherz	Avg fertile harz	Avg depl harz	Avg fertile gt sp lherz	Avg depl gt sp lherz	Avg sili metas gt sp lherz	Avg fertile wehr	Avg depl wehr
n	4	40	29	19	2	7	10	4	3	9	4
SiO_2	41.40	41.08	41.70	41.07	39.90	40.09	41.46	41.53	41.53	41.30	40.38
TiO_2	0.22	0.09	0.44	0.09	0.08	0.14	0.06	0.04	0.05	0.08	0.04
Al_2O_3	19.55	19.12	20.40	19.06	11.65	12.46	22.22	22.10	22.67	22.16	16.98
Cr_2O_3	5.27	6.12	3.85	6.39	15.25	14.06	2.36	2.60	2.09	2.35	8.50
FeO^{total}	8.39	7.63	8.06	7.69	6.79	7.00	9.02	8.75	9.68	9.56	8.39
MnO	0.43	0.43	0.36	0.43	0.38	0.38	0.51	0.55	0.51	0.52	0.51
MgO	19.35	19.00	20.11	19.02	18.60	18.41	18.65	18.90	18.33	18.14	16.93
CaO	5.63	6.19	5.02	6.07	6.91	6.87	5.70	5.64	5.57	6.04	7.96
Na_2O	0.02	0.03	0.07	0.04	0.04	0.03	0.03	0.02	0.02	0.04	0.06
Total	100.3	99.7	100.0	99.9	99.6	99.4	100.0	100.1	100.5	100.2	99.7
Mg#	80.4	81.6	81.6	81.5	83.0	82.4	78.7	79.4	77.1	77.2	78.3
Cr#	15.4	17.7	11.3	18.4	46.8	43.2	6.7	7.3	5.8	6.7	25.2

Average major element composition of different classes of garnet xenocrysts (analyses of Griffin et al., 2004) in wt.%; the basis for the classification is the Cr–Ca relationship (lherzolite, harzburgite, garnet–spinel lherzolite, wehrlite) combined with Zr–Y relationships (used to distinguish fertile, depleted, silicate-metasomatised and "phlogopite"-metasomatised sources; Griffin et al., 1999a); *n*: number of grains averaged; avg: average; depl: depleted; sili metas: silicate melt metasomatised; phlog met: "phlogopite"-metasomatised; wehr: wehrlite; for other abbreviations see Table 2.

the lherzolite field, with Cr_2O_3 contents up to ~ 10 wt.% (group 1). A second group (group 2) scatters toward higher CaO contents at a given Cr_2O_3 content. This is similar to what is observed for spinel-bearing garnet peridotites from the north-central Slave craton, which were interpreted to be less strongly enriched in Cr_2O_3 at a given CaO content due to coexisting high-Cr spinel (Kopylova et al., 2000). The group of garnets with the highest Cr_2O_3 contents (14–18 wt.%) plots parallel to the lherzolite field but is displaced toward lower CaO contents (group 3).

One group of garnets, which includes those from garnet spinel lherzolite where spinel and garnet share high-energy amoeboid grain boundaries, is restricted to low Cr_2O_3 contents (~ 1.5–3 wt.%; group 4). This group may represent peridotites from the garnet spinel transition zone. The higher abundance of spinel and the presence of Cr-rich orthopyroxene in these samples, compared to chromite-bearing garnet peridotites, may limit the uptake of Cr_2O_3 in coexisting garnet. Garnets in pyroxenite xenoliths from Buffalo Hills have <1 wt.% Cr_2O_3 and show a steeper correlation between Cr_2O_3 and CaO contents than those in peridotites.

Garnets in peridotite xenoliths have TiO_2 contents up to 0.79 wt.%, Cr_2O_3 from 2.00 to 6.96 wt.% and CaO from 4.61 to 6.50 wt.%. The highest TiO_2 contents are observed in the sheared lherzolite K14-1. Mg-numbers [Mg#: $100Mg/(Mg + Fe)$] range from 71.9 to 84.3. Garnet in garnet spinel lherzolite K14-3a has the lowest Mg-number and Cr-number [Cr#: $100Cr/(Cr + Al)$]. Of the 26 spot analyses sampling five garnets in garnet harzburgite K11-5, 21 gave a Ca-saturated lherzolitic composition (CaO = 6.5 ± 0.19 wt.%). Five analyses in two of the garnets gave a Ca-undersaturated composition, with distinctly and relatively uniform lower CaO (4.1 ± 0.34 wt.%) and higher TiO_2 content.

Garnets from pyroxenite xenoliths have lower TiO_2 contents (<0.06–0.08) and Cr_2O_3 contents (0.09–1.00 wt.%) than peridotitic garnets, and CaO varies from 4.69 to 5.90 wt.%. Mg-numbers range from 62.2 to 70.3 and do not overlap those of peridotitic garnets. The pyroxenite with corona structure has garnets with unequilibrated major-element composition, depending on their position relative to the broad garnet corona. Average, minimum and maximum values are given in Table 2. Garnet arranged in necklaces around orthopyroxene in the orthopyroxene-rich domain (domain 2) and garnet of the corona have average CaO of 5.40 and 4.83 wt.%, respectively, and Mg-numbers of 64.5 and 69.1, respectively.

Table 4
Representative major-element composition of clinopyroxene

Sample	K6-2b	K6-2b	K6-2b	K6-3	K6-4	K6-5b	K14-1	K14-2a	K14-2a
n	20	10	20	14	15	20	22	18	6
Comment	core	rim	20 mic		core			core	rim
Type	sp lherz	sp lherz	sp lherz	sp lherz	sp lherz	pyrox	gt lherz	gt pyrox	gt pyrox
SiO_2	53.55	53.78	53.31	55.07	54.95	52.89	55.01	53.80	54.14
TiO_2	<0.06	<0.06	<0.06	<0.06	<0.06	0.42	0.21	0.33	0.28
Al_2O_3	2.55	2.08	2.54	2.28	2.76	5.68	1.79	4.88	4.25
Cr_2O_3	0.90	0.75	0.90	0.81	0.98	0.91	1.01	0.33	0.36
FeO^{total}	1.74	1.70	1.82	1.58	1.71	3.43	3.80	2.75	2.50
MnO	<0.09	<0.09	<0.09	<0.09	<0.09	<0.09	0.10	<0.09	<0.09
MgO	16.72	17.02	17.16	16.63	16.52	14.03	18.62	14.82	15.07
CaO	23.73	23.91	23.28	24.15	23.60	22.11	17.46	22.09	22.52
NiO	<0.08	<0.08	<0.08	<0.08	<0.08	<0.08	<0.08	<0.08	<0.08
Na_2O	0.56	0.53	0.57	0.47	0.63	1.40	1.61	1.45	1.39
K_2O	<0.04	<0.04	<0.04	<0.04	<0.04	<0.04	<0.04	<0.04	<0.04
Total	99.9	100.0	99.8	101.1	101.3	101.0	99.7	100.5	100.6
Mg#	94.5	94.7	94.4	94.9	94.5	87.9	89.7	90.6	91.5
Cr#	19.1	19.5	19.2	19.3	19.2	9.7	28.2	4.4	5.5

Sample	K14-2c	K14-2c	K14-2c	K14-3a	K14-3b2	K14-5b	K14-5c (4) max	K14-5c (4) min	K14-5c (4) avg
n	12	6	15	17	12	33			10
Comment	core	rim	20 mic				domain 4	domain 4	domain 4
Type	sp lherz	sp lherz	sp lherz	gt lherz	perid	sp lherz	gt pyrox	gt pyrox	gt pyrox
SiO_2	53.72	54.21	53.64	54.64	54.59	53.62	55.27	52.87	54.32
TiO_2	<0.06	<0.06	<0.06	0.11	0.19	0.07	1.83	0.15	0.51
Al_2O_3	2.34	1.84	2.31	1.66	0.75	1.75	5.03	2.71	4.23
Cr_2O_3	0.90	0.62	0.81	0.70	1.14	0.63	0.17	<0.09	0.09
FeO^{total}	1.82	1.74	1.89	1.75	2.75	1.44	3.63	2.38	3.04
MnO	<0.09	<0.09	<0.09	<0.09	<0.09	<0.09	<0.09	<0.09	<0.09
MgO	16.80	17.35	17.31	17.30	17.62	16.94	16.60	14.27	14.97
CaO	23.82	23.88	23.27	23.62	21.95	24.28	24.06	22.03	22.50
NiO	<0.08	<0.08	<0.08	<0.08	<0.08	<0.08	<0.08	<0.08	<0.08
Na_2O	0.52	0.48	0.49	0.65	0.77	0.61	1.80	0.33	1.40
K_2O	<0.04	<0.04	<0.04	<0.04	<0.04	<0.04	<0.04	<0.04	<0.04
Total	100.1	100.2	99.9	100.5	99.9	99.5	101.4	100.8	101.1
Mg#	94.3	94.7	94.2	94.6	92.0	95.5	91.9	87.7	89.8
Cr#	20.4	18.3	19.0	21.4	50.4	19.3	2.7	0.6	1.5

Sample	K14-5c (5) max	K14-5c (5) min	K14-5c (5) avg	K14-6	K14-6	K14-6	K14-7a	K14-7a	K14-7a
n			12	25	3	20	17	10	30
Comment	domain 5	domain 5	domain 5		incl	20 mic	core	rim	20 mic
Type	gt pyrox	gt pyrox	gt pyrox	sp lherz	sp lherz	sp lherz	sp lherz	sp lherz	sp lherz
SiO_2	55.06	52.90	54.45	52.94	53.49	53.42	53.63	53.81	53.34
TiO_2	0.57	0.34	0.47	<0.06	0.06	<0.06	0.17	0.15	0.19
Al_2O_3	6.02	5.25	5.61	2.63	2.01	2.56	2.78	2.11	3.10
Cr_2O_3	0.14	<0.09	<0.09	0.91	0.74	0.89	1.08	0.87	1.17
FeO^{total}	5.17	2.51	3.19	1.78	1.47	1.89	1.44	1.91	1.56
MnO	<0.09	<0.09	<0.09	<0.09	<0.09	<0.09	<0.09	<0.09	<0.09
MgO	16.51	13.97	14.48	16.52	16.71	16.95	16.25	17.28	16.57
CaO	21.50	18.06	20.78	23.79	24.36	23.38	23.59	23.00	22.96
NiO	<0.08	<0.08	<0.08	<0.08	<0.08	<0.08	<0.08	<0.08	<0.08

Table 4 (*continued*)

Sample	K14-5c (5) max	K14-5c (5) min	K14-5c (5) avg	K14-6	K14-6	K14-6	K14-7a	K14-7a	K14-7a
n			12	25	3	20	17	10	30
Comment	domain 5	domain 5	domain 5		incl	20 mic	core	rim	20 mic
Type	gt pyrox	gt pyrox	gt pyrox	sp lherz	sp lherz	sp lherz	sp lherz	sp lherz	sp lherz
Na_2O	2.25	1.70	2.13	0.55	0.54	0.55	1.04	0.80	1.08
K_2O	0.14	<0.04	<0.04	<0.04	<0.04	<0.04	<0.04	<0.04	<0.04
Total	101.8	100.6	101.3	99.3	99.5	99.8	100.1	100.0	100.1
Mg#	91.1	83.7	89.1	94.3	95.3	94.1	95.3	83.8	95.0
Cr#	1.7	0.3	1.0	18.7	19.9	18.8	20.9	19.2	20.1

Representative major-element composition of clinopyroxene in wt.%; 20 mic denotes cpx with exsolved opx analysed with 20 μm electron beam; incl: inclusion; for other abbreviations and explanations, see Table 2.

5.2. Clinopyroxene

Clinopyroxenes in spinel lherzolites have Al_2O_3 from 1.75 to 3.34 wt.%, Cr_2O_3 from 0.62 to 1.08 wt.% and Na_2O from 0.44 to 1.05 wt.% (Fig. 4). Mg-numbers range from 91.3 to 95.5. Clinopyroxene in the sheared lherzolite has a distinctly lower Mg-number and higher FeO, MgO, Na_2O and TiO_2 contents than other peridotites, while also having the lowest CaO of all samples.

Compared to peridotites, clinopyroxenes in pyroxenites have higher Al_2O_3 (2.71–6.30 wt.%) and Na_2O (0.33–2.25 wt.%) and lower Cr_2O_3 contents (<0.09–0.91 wt.%). Mg-numbers are lower and more variable than for peridotitic garnets (82.6–92.1). Garnet-free pyroxenites have the highest Al_2O_3 and Cr_2O_3 contents. Like garnet, clinopyroxenes in the corona-structured pyroxenite have differing compositions, depending on their position in the sample. Clinopyroxenes within the corona (coarse-grained domain) has Al_2O_3 and CaO contents of 4.72 and 22.08 wt.%, respectively, compared to 5.61 and 20.78 wt.%, respectively, for clinopyroxene outside the corona (fine-grained domain). Cr_2O_3 contents in clinopyroxenes of the corona-structured pyroxenite are the lowest of all samples analysed in this study, on average below the detection limit (0.09 wt.%), whereas Na_2O contents are highest for the corona-structured pyroxenite, with 1.40 wt.% for clinopyroxene within and 2.13 wt.% for clinopyroxene outside the garnet corona.

Some clinopyroxenes have rim compositions that differ from those in the cores. Al_2O_3, Cr_2O_3 and Na_2O contents of clinopyroxene rims are higher than in the cores in most cases. Clinopyroxene occurs as inclusions in olivine, orthopyroxene and garnet. Included grains have lower Al_2O_3 and Cr_2O_3 contents and higher CaO contents than non-included grains in the same sample, while their TiO_2 and Na_2O contents and Mg-numbers show no appreciable difference. Many clinopyroxenes contain exsolution lamellae of both orthopyroxene and spinel. Compositions prior to the exsolution were estimated by averaging 20–30 analyses obtained with a defocused microbeam, sampling an area ca 20 μm wide. Pre-exsolution clinopyroxenes tend to have higher Al_2O_3 and lower CaO contents than postexsolution clinopyroxenes, while TiO_2 and Na_2O are indistinguishable.

5.3. Orthopyroxene

Orthopyroxenes in spinel lherzolites have Al_2O_3 contents ranging from 2.20 to 3.07 wt.%, Cr_2O_3 from 0.33 to 0.55 wt.% and CaO from 0.23 to 1.10 wt.%. Mg-numbers lie between 91.3 and 92.0. CaO contents are generally lower than in garnet peridotites. This is consistent with derivation from the spinel stability field, and hence lower temperatures (Brey and Köhler, 1990). Orthopyroxene from the sheared garnet lherzolite has the lowest Mg-number and the lowest Al_2O_3, Cr_2O_3 and MgO contents of all peridotites. It has high CaO (1.0 wt.%) and Na_2O content (0.25 wt.%). Orthopyroxene from the garnet spinel peridotite has Al_2O_3, Cr_2O_3 and CaO contents intermediate between the sheared garnet lherzolite and spinel lherzolites. Orthopyroxene in garnet pyroxenite generally has higher Al_2O_3

Table 5
Representative major-element composition of orthopyroxene

Sample	K6-2b	K6-2b	K6-3	K6-3	K6-4	K6-5b	K14-1	K14-2a
n	18	16	4	8	5	17	26	13
Comment		20 mic		20 mic				
Type	sp lherz	sp lherz	sp lherz	sp lherz	sp lherz	pyrox	gt lherz	gt pyrox
SiO_2	56.15	56.12	57.52	56.32	57.71	55.02	57.67	56.75
TiO_2	<0.06	<0.06	<0.06	<0.06	<0.06	<0.06	0.12	<0.06
Al_2O_3	2.66	2.68	2.46	2.66	2.46	4.60	0.73	2.47
Cr_2O_3	0.55	0.54	0.46	0.52	0.46	0.51	0.19	0.15
FeO^{total}	5.54	5.43	5.68	5.61	5.54	10.21	5.98	8.08
MnO	0.11	0.14	0.13	0.15	0.12	0.22	0.12	0.11
MgO	34.53	34.62	34.58	34.41	34.48	30.28	34.15	33.09
CaO	0.57	0.61	0.31	0.51	0.35	0.25	1.00	0.20
NiO	0.08	0.09	<0.08	0.09	0.10	<0.08	0.13	<0.08
Na_2O	<0.04	<0.04	<0.04	<0.04	<0.04	<0.04	0.25	<0.04
K_2O	<0.04	<0.04	<0.04	<0.04	<0.04	<0.04	<0.04	<0.04
Total	100.3	100.3	101.2	100.3	101.2	101.2	100.4	100.9
Mg#	91.7	91.9	91.6	91.6	91.7	84.1	91.1	88.0
Cr#	12.2	12.0	11.0	11.6	11.1	7.0	14.8	3.8

Sample	K14-2c	K14-2c	K14-2c	K14-3a	K14-5b	K14-5b	K14-5c (2) max	K14-5c (2) min
n	22	12	2	33	21	30		
Comment	core	rim	20 mic			20 mic	domain 2	domain 2
Type	sp lherz	sp lherz	sp lherz	gt lherz	sp lherz	sp lherz	gt pyrox	gt pyrox
SiO_2	56.48	56.75	56.48	57.62	56.06	56.13	57.05	55.79
TiO_2	<0.06	<0.06	<0.06	<0.06	<0.06	<0.06	0.08	<0.06
Al_2O_3	2.53	2.31	2.48	1.40	2.20	2.69	3.12	1.70
Cr_2O_3	0.54	0.47	0.51	0.31	0.33	0.50	0.14	<0.09
FeO^{total}	5.52	5.59	5.40	5.75	5.68	5.68	9.95	9.03
MnO	0.13	0.12	0.12	0.11	0.13	0.13	0.14	<0.09
MgO	34.52	34.80	34.77	35.22	34.85	35.00	33.16	31.28
CaO	0.62	0.42	0.56	0.18	0.30	0.39	0.58	0.14
NiO	<0.08	<0.08	0.08	0.08	<0.08	<0.08	0.09	<0.08
Na_2O	<0.04	<0.04	<0.04	<0.04	<0.04	<0.04	0.09	<0.04
K_2O	<0.04	<0.04	<0.04	<0.04	<0.04	<0.04	<0.04	<0.04
Total	100.4	100.5	100.4	100.7	99.7	100.6	101.5	100.4
Mg#	91.8	91.7	92.0	91.6	91.6	91.7	86.5	85.1
Cr#	12.5	11.9	12.2	11.5	9.2	10.9	3.7	0.0

Sample	K14-5c (2) avg	K14-5c2	K14-6	K14-6	K14-7a	K14-7a		
n	32	22	31	23	34	29		
Comment	domain 2			20 mic		20 mic		
Type	gt pyrox	pyrox	sp lherz	sp lherz	sp lherz	sp lherz		
SiO_2	56.45	53.59	55.93	56.32	56.59	56.45		
TiO_2	<0.06	0.06	<0.06	<0.06	0.06	<0.06		
Al_2O_3	2.32	5.24	2.43	2.66	2.26	2.32		
Cr_2O_3	<0.09	0.47	0.42	0.50	0.47	0.53		
FeO^{total}	9.49	9.57	5.63	5.62	5.47	5.48		
MnO	<0.09	0.19	0.14	0.15	0.13	0.12		
MgO	32.30	30.90	34.31	34.28	35.25	35.29		
CaO	0.21	0.23	0.42	0.52	0.32	0.40		
NiO	<0.08	<0.08	0.08	0.09	<0.08	0.08		
Na_2O	<0.04	<0.04	<0.04	<0.04	<0.04	<0.04		

Table 5 (*continued*)

Sample	K14-5c (2) avg	K14-5c2	K14-6	K14-6	K14-7a	K14-7a
n	32	22	31	23	34	29
Comment	domain 2			20 mic		20 mic
Type	gt pyrox	pyrox	sp lherz	sp lherz	sp lherz	sp lherz
K_2O	<0.04	<0.04	<0.04	<0.04	<0.04	<0.04
Total	101.0	100.3	99.4	100.2	100.6	100.8
Mg#	85.9	85.2	91.6	91.6	92.0	92.0
Cr#	1.7	5.6	10.3	11.2	12.1	13.3

Representative major-element composition of orthopyroxene in wt.%; for abbreviations, see Tables 2 and 4.

(2.31–3.63 wt.%) and lower Cr_2O_3 (<0.09–0.53 wt.%), CaO contents (0.15–0.58 wt.%) and Mg-number (85.1–88.5) than peridotitic orthopyroxene.

Orthopyroxene in garnet-free pyroxenite ranges to even higher Al_2O_3, FeO and lower MgO contents and has the lowest Mg-number of all samples (84.1).

Table 6
Representative major-element composition of olivine

Sample	K6-2b	K6-2b	K6-3	K6-4	K6-4	K11-5	K11-6
n	18	6	21	14	2	21	3
Comment	core	rim			incl in opx		
Type	sp lherz	sp lherz	sp lherz	sp lherz	sp lherz	alt gt harz	alt gt harz
SiO_2	40.94	40.60	41.98	41.91	42.10	41.04	41.23
TiO_2	<0.06	<0.06	<0.06	<0.06	<0.06	<0.06	<0.06
Al_2O_3	<0.03	<0.03	<0.03	<0.03	<0.03	<0.03	<0.03
Cr_2O_3	<0.09	<0.09	<0.08	<0.05	<0.04	<0.09	<0.09
FeO^{total}	8.53	8.26	8.44	8.41	8.21	8.29	7.80
MnO	0.12	0.12	0.13	0.13	0.10	0.12	0.11
MgO	50.60	50.01	50.16	50.38	50.42	50.92	50.64
CaO	<0.05	<0.05	<0.05	<0.05	<0.05	<0.05	<0.05
NiO	0.40	0.39	0.39	0.39	0.49	0.36	0.41
Na_2O	<0.04	<0.04	<0.04	<0.04	<0.04	<0.04	<0.04
K_2O	<0.04	<0.04	<0.04	<0.04	<0.04	<0.04	<0.04
Total	100.7	99.5	101.2	101.3	101.4	100.8	100.3
Mg#	91.4	91.5	91.4	91.4	91.6	91.6	92.1
Sample	K14-1	K14-2c	K14-3a	K14-3b2	K14-5b	K14-6	K14-7a
n	44	24	25	17	44	27	26
Comment							
Type	gt lherz	sp lherz	gt sp lherz	perid	sp lherz	sp lherz	sp lherz
SiO_2	40.86	41.09	40.89	40.97	40.38	40.29	41.20
TiO_2	<0.06	<0.06	<0.06	<0.06	<0.06	<0.06	<0.06
Al_2O_3	<0.03	<0.03	<0.03	<0.03	<0.03	<0.03	<0.03
Cr_2O_3	<0.09	<0.09	<0.09	<0.09	<0.09	<0.09	<0.09
FeO^{total}	9.91	8.50	8.65	9.18	8.38	8.56	8.12
MnO	0.11	0.12	0.11	0.11	0.11	0.12	0.09
MgO	49.09	50.45	50.56	49.63	50.63	50.08	51.21
CaO	0.05	<0.05	<0.05	<0.05	<0.05	<0.05	<0.05
NiO	0.39	0.39	0.37	0.38	0.37	0.43	0.37
Na_2O	<0.04	<0.04	<0.04	<0.04	<0.04	<0.04	<0.04
K_2O	<0.04	<0.04	<0.04	<0.04	<0.04	<0.04	<0.04
Total	100.5	100.6	100.6	100.4	99.9	99.5	101.1
Mg#	89.8	91.4	91.2	90.6	91.5	91.2	91.8

Representative major-element composition of olivine in wt.%; for abbreviations, see Tables 2 and 4.

Table 7
Representative major-element composition of spinel

Sample	K6-2b	K6-2b	K6-2b	K6-2b	K6-3	K6-3	K6-4
n	11	6	6	6	21	9	16
Comment	core	rim	skeletal	overgr	core	rim	core
Type	sp lherz	sp lherz	sp lherz	sp lherz	sp lherz	sp lherz	sp lherz
SiO_2	0.10	0.16	0.38	0.57	<0.07	<0.07	<0.07
TiO_2	<0.06	<0.06	2.65	0.09	<0.06	<0.06	<0.06
Al_2O_3	35.78	35.62	11.87	28.68	36.81	36.91	37.58
Cr_2O_3	31.97	31.33	42.99	37.99	31.30	30.97	30.84
FeO	12.17	11.21	14.06	10.51	13.29	12.57	11.92
Fe_2O_3	2.74	2.99	11.88	4.87	1.74	2.10	2.15
MnO	0.23	0.19	0.34	0.19	0.22	0.21	0.19
MgO	16.23	16.64	14.35	17.24	15.50	15.95	16.58
CaO	<0.05	0.06	0.09	<0.05	<0.05	<0.05	<0.05
NiO	0.10	0.12	0.09	0.06	0.12	0.12	0.13
ZnO	0.29	0.35	0.13	0.26	0.26	0.26	0.27
V_2O_5	0.17	0.16	0.06	0.21	0.15	0.16	0.15
Total	99.8	98.9	98.9	100.7	99.5	99.3	99.9
Mg#	66.4	68.1	50.8	67.4	65.0	66.3	68.1
Cr#	37.5	37.1	70.3	47.2	36.3	36.0	35.5
Fe^{3+}#	16.9	19.4	42.7	29.1	10.5	13.1	14.0

Sample	K6-4	K6-4	K14-3a	K14-3a	K14-3a	K14-3a	K14-5b
n	6	7	4	4	9	4	7
Comment	rim	overgr	contact w/ilm	contact w/sulf	incl type I	incl type II	core
Type	sp lherz	sp lherz	gt sp lherz	gt sp lherz	gt sp lherz	gt sp lherz	sp lherz
SiO_2	0.10	0.15	0.12	0.10	0.07	0.08	<0.07
TiO_2	<0.06	0.06	1.33	0.27	0.29	0.16	<0.06
Al_2O_3	35.73	33.02	26.99	27.24	30.56	39.22	39.26
Cr_2O_3	32.11	34.69	36.16	37.59	33.97	26.65	28.34
FeO	10.13	9.62	17.80	14.78	15.42	12.89	11.79
Fe_2O_3	3.54	4.31	4.04	5.62	5.10	4.35	3.70
MnO	0.20	0.14	0.27	0.45	0.22	0.21	0.20
MgO	17.61	17.83	12.47	13.80	13.79	16.32	17.14
CaO	<0.05	<0.05	<0.05	<0.05	<0.05	<0.05	<0.05
NiO	0.17	0.18	0.14	0.38	0.13	0.21	0.14
ZnO	0.28	0.23	0.24	0.14	0.34	0.39	0.29
V_2O_5	0.13	0.16	na	na	na	na	na
Total	100.1	100.4	99.6	100.4	99.9	100.5	100.9
Mg#	70.2	70.2	50.9	55.4	55.1	63.4	66.9
Cr#	37.7	41.4	47.3	48.1	42.7	31.3	32.6
Fe^{3+}#	23.9	28.7	17.0	25.5	22.9	23.3	22.1

Sample	K14-5b	K14-5b	K14-5b	K14-6	K14-6	K14-6	K14-7a
n	3	11	8	20	12	10	5
Comment	rim	incl in opx	overgr	core	rim	overgr	incl in ol
Type	sp lherz	sp lherz	sp lherz	sp lherz	sp lherz	sp lherz	sp lherz
SiO_2	<0.07	<0.07	0.11	0.09	0.08	0.15	<0.07
TiO_2	<0.06	0.07	0.19	0.06	0.07	0.10	0.17
Al_2O_3	39.60	38.82	33.91	38.57	38.08	32.52	32.34
Cr_2O_3	27.80	28.22	33.61	30.22	30.53	34.39	36.01
FeO	10.40	11.06	8.76	12.51	11.87	11.39	9.42
Fe_2O_3	4.05	4.12	5.49	1.81	2.41	4.77	4.03
MnO	0.15	0.14	0.18	0.19	0.20	0.18	0.14

(continued on next page)

Table 7 (*continued*)

Sample	K14-5b	K14-5b	K14-5b	K14-6	K14-6	K14-6	K14-7a
n	3	11	8	20	12	10	5
Comment	rim	incl in opx	overgr	core	rim	overgr	incl in ol
Type	sp lherz	sp lherz	sp lherz	sp lherz	sp lherz	sp lherz	sp lherz
MgO	18.03	17.55	18.86	16.57	16.96	16.83	18.05
CaO	<0.05	<0.05	<0.05	<0.05	<0.05	<0.05	<0.05
NiO	0.12	0.14	0.20	0.12	0.13	0.14	0.15
ZnO	0.24	0.21	0.20	0.29	0.28	0.25	0.25
V_2O_5	na	na	na	na	na	na	na
Total	100.5	100.4	101.5	100.4	100.6	100.7	100.6
Mg#	69.6	67.9	71.0	67.6	68.3	65.7	71.1
Cr#	32.0	32.8	40.0	34.5	35.0	41.5	42.8
Fe^{3+}#	26.0	25.2	36.1	11.5	15.4	27.3	27.8

Representative major-element composition of spinel in wt.%; Fe^{3+}# = molar (100 Fe^{3+}/(Fe^{3+} + Fe^{2+}) after Droop (1987); overgr: overgrowth; w/ilm: with ilmenite; w/sulf: with sulfide; na: not analysed or not available; for other abbreviations, see Tables 2 and 4.

Like clinopyroxene, many orthopyroxenes contain exsolution lamellae of the complementary pyroxene and of spinel. Orthopyroxenes after exsolution have lower Al_2O_3 and CaO contents, while Mg-numbers are mostly comparable.

5.4. Olivine

Mg-numbers of olivine in spinel lherzolites show little variation (91.0 to 91.8). The sheared garnet lherzolite has the lowest Mg-number (89.8) and garnet

spinel lherzolite has a low Mg-number (91.2). Garnet peridotites with altered pyroxene, which are assumed to be garnet harzburgites, trend towards the highest Mg-numbers (91.6 to 92.9) and have NiO contents ranging from 0.36 to 0.41 wt.%. There are no covariations between Mg-number and NiO or MnO content.

5.5. Spinel

Spinel in many xenoliths consists of primary spinel cores and secondary overgrowths (see Fig. 14B).

Table 8
Major-element composition of rutile and ilmenite

Sample	K14-2a	K14-5c	K14-5c	K14-2a	K14-3a	K14-5c
	rutile	rutile	rutile	ilmenite	ilmenite	ilmenite
n	8	8	4	3	4	1
Comment			incl in cpx	rim on rut		rim on rut
Type	gt pyrox	gt pyrox	gt pyrox	gt pyrox	gt sp lherz	gt pyrox
SiO_2	0.10	<0.07	0.08	0.13	0.50	0.05
TiO_2	97.50	98.58	98.29	54.94	53.77	56.87
Al_2O_3	0.16	0.25	0.21	0.30	0.83	0.60
Cr_2O_3	0.55	0.13	0.13	0.65	2.15	0.22
FeO	0.34	0.59	1.07	32.87	27.81	31.36
Fe_2O_3	na	na	na	na	1.17	
MnO	<0.09	<0.09	<0.09	0.75	0.50	0.58
MgO	<0.06	<0.06	<0.06	9.12	11.32	9.25
CaO	0.07	0.07	<0.05	0.21	0.19	0.10
NiO	<0.08	<0.08	<0.08	<0.08	0.16	<0.08
ZnO	<0.04	<0.04	<0.04	<0.04	<0.04	0.10
V_2O_5	0.31	0.65	0.44	0.23	<0.04	0.53
Total	99.1	100.4	100.3	99.0	98.4	99.7
Mg#	na	na	na	33.1	57.9	65.5
Cr#	71.9	23.2	29.5	58.9	63.7	19.9

Major-element composition of rutile and ilmenite in wt.%; na: not analysed or not available; for other abbreviations and explanations, see Tables 2 and 4.
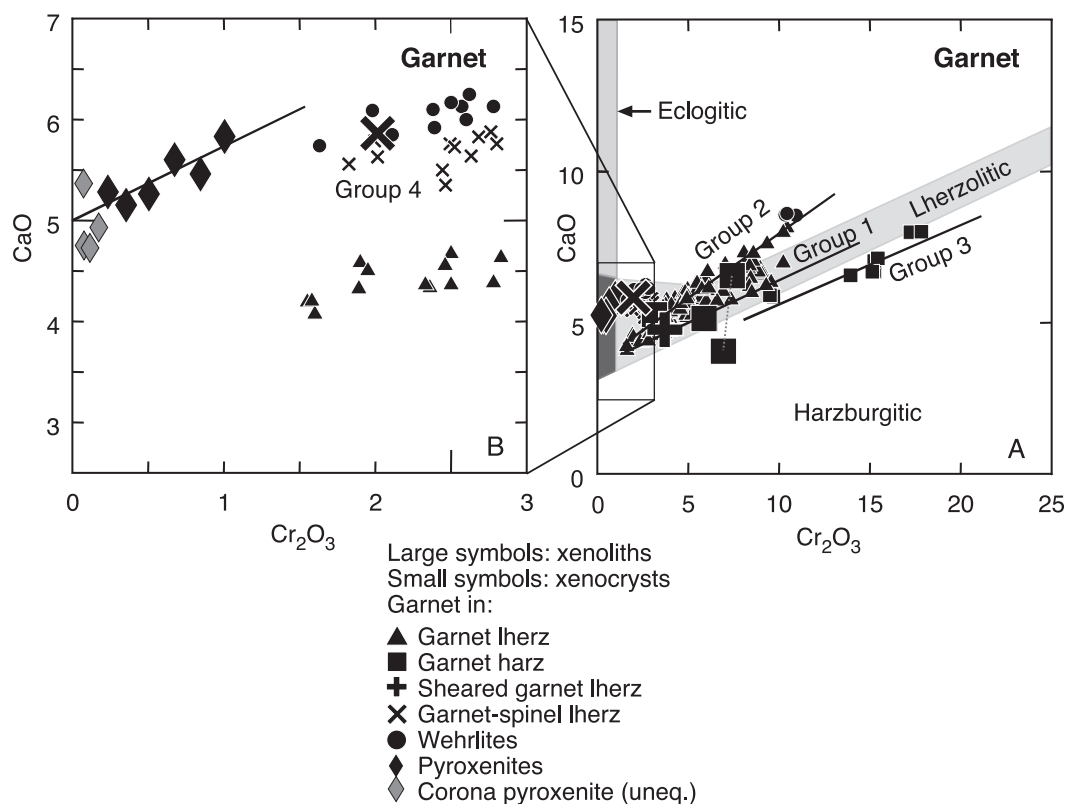
Fig. 3. Cr_2O_3 against CaO (wt.%) in garnet. Xenocrysts from Griffin et al. (2004), fields of Sobolev et al. (1973) and Gurney (1984). Stippled line connects two compositionally distinct garnet populations in sample K11-5. Diagram on the left represents the enlarged area of the rectangle shown in the diagram on the right. Groups 1 to 4 are discussed in the text.

Core–rim zonations are commonly observed, as are skeletal growth textures. Spinel is assumed to be primary in origin if it has TiO_2 contents from <0.06 to 0.11 wt.%, ZnO from 0.25 to 0.34 wt.%, Mg-number from 63.1 to 71.3, Cr-number from 29.0 to 40.6 and Fe^{3+}-number [Fe^{3+}#: $100Fe^{3+}/(Fe^{3+}+Fe^{2+})$] from 9.2 to 28.4. By contrast, secondary overgrowths on spinel trend towards substantially higher TiO_2 contents (0.06–3.43 wt.%), Cr-numbers (36.6–79.6) and Fe^{3+}-numbers (22.7–54.1) and lower ZnO contents (0.06–0.34 wt.%) and Mg-numbers (49.6–72.4). Zn contents in mantle spinel are inversely correlated with temperature (Griffin et al., 1994), and the lower ZnO contents recorded for many of the secondary overgrowths could indicate that they formed in a hotter environment than primary spinel cores. Rim compositions of spinels vary according to the composition of the phase with which they are in contact. For

example, spinel next to ilmenite contains significantly more TiO_2, whereas spinel adjacent to sulfide contains more NiO than spinel adjacent to silicate phases (sample K14-3a).

5.6. Rutile and ilmenite

Rutile occurs in two garnet pyroxenites, one of which has the corona structure described above. Oxides of Al, Cr, Fe and V are present at levels between 0.13 and 1.07 wt.%. Rutile shows minor ilmenite exsolution. One small ilmenite grain occurs in the garnet spinel peridotite. It has an Mg-number of 57.9 and Cr-number of 63.7.

5.7. Sulfide

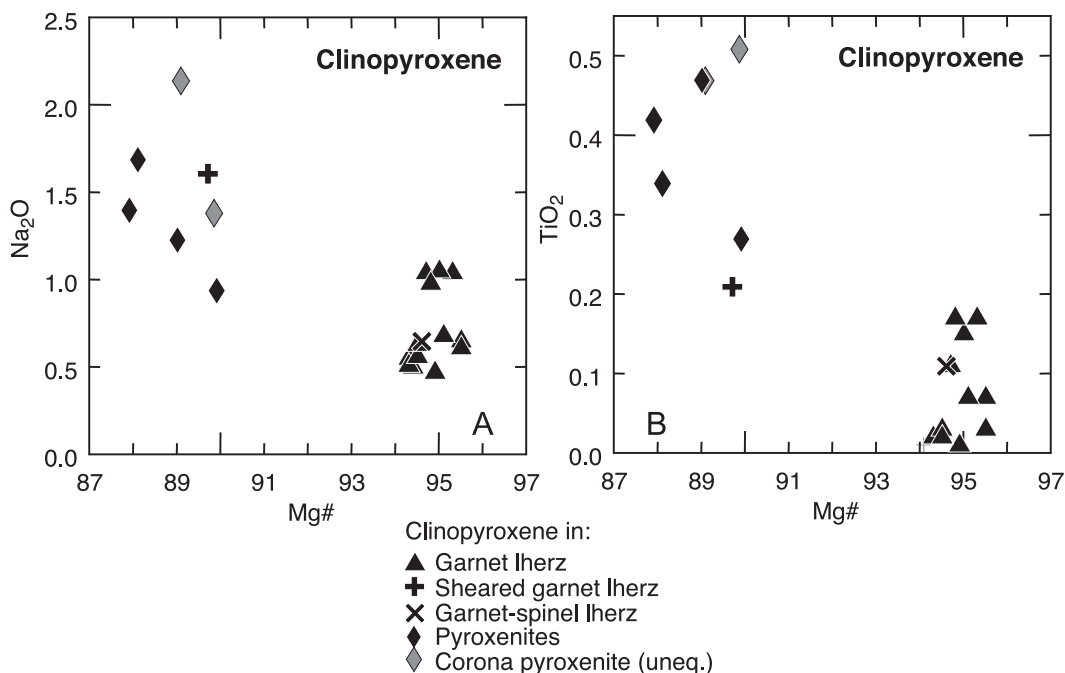Bulk sulfides were reconstructed from low-temperature assemblages using mineral compositions

Fig. 4. Mg-number (Mg#) against (A) Na_2O and (B) TiO_2 in cpx.

and modal abundances. Their grain sizes, shapes and low-temperature mineral assemblages are given in Table 9. Sulfides in spinel lherzolites and in pyroxenites are mostly single-phase pentlandites and reconstructed sulfur-poor (?altered) monosulfide solid solution (mss). Two pyroxenites contain chalcosite (Cu_2S). Ni- and Co-rich sulfide occurs in one spinel lherzolite and in a pyroxenite, where it coexists with mss and pentlandite. Sulfide is unusually abundant in the garnet spinel lherzolite (K14-3a), suggesting a secondary origin during influx of sulfur. Spinel lherzolite K14-5b contains a melt patch, half of which is occupied by an aggregate of polygonal pentlandites. A spherical pendlandite grain occurs in another melt patch in the same sample. Many sulfides contain high amounts of Si (up to 4.2 wt.%), which are possibly due to silicate melt inclusions. Most sulfides have high O contents (up to 16.1 wt.%) regardless of their Si contents, and this is ascribed to oxidation and alteration of the sulfides, although discrete secondary minerals, such as hematite, are not observed.

5.8. Melt

The major-element composition of the melt patch in sample K14-5b is difficult to estimate because it contains large oxide and sulfide phenocrysts, which appear to have crystallised from this melt. Phenocryst-free areas contain 43.1 wt.% SiO_2, 0.81 wt.% Al_2O_3, 4.6 wt.% FeO, 38.9 wt.% MgO, 0.11 wt.% CaO and 0.13 wt.% NiO; TiO_2, Na_2O and K_2O are below detection limits (0.07, 0.04 and 0.04 wt.%, respectively). The sum from the microprobe analysis is only 88 wt.%, and trace-element analyses have not revealed any elements at concentrations higher than in the thousands of ppm. This suggests that light elements, such as carbon and/or hydrogen, may be present.

6. Trace elements

6.1. Garnet

Representative trace-element data for xenolithic garnets and clinopyroxenes, and for the melt patch

Table 9
Representative characteristics and major-element composition of sulfide

Sample n	K6-1	K6-5b-2	K6-5b-3	K14-2a	K14-2ba	K14-3a	K14-5b	K14-5d	K14-6	K14-7a
Context	i	e opx	i	e cpx	e ol	i+e opx+e ol	i melt	i	i	e opx
Grain size [μm]	125	120	100	50	70	div	div	95	455	155
Shape	irregular	elongate	elongate– irregular	irregular	polyhedral	polyhedral/ spherical	polyhedral/ spherical	polyhedral	polyhedral	spherical
Mineral/ assemblage	pn	mss	gs–hz	cs	mss	pn	pn	pn	pn	pn
Lithotype	sp lherz	gt pyrox	gt pyrox	gt pyrox	sp lherz	grt lherz	sp lherz	sp lherz	sp lherz	sp lherz
Cu	0.5	2.9	3.1	58.3	13.4	3.2	2.6	0.9	2.4	1.4
Fe	27.9	46.0	4.0	3.6	26.4	33.5	30.6	26.5	31.3	32.0
Ni	37.4	13.1	44.3	1.2	23.3	22.3	23.9	24.0	29.2	25.7
Co	0.7	0.7	5.4	0.1	0.5	0.5	0.6	0.5	0.6	0.6
S	32.0	33.5	21.4	15.9	27.8	27.2	27.1	24.7	29.2	28.7
Si	0.2	<0.07	na	na	1.2	1.2	2.1	4.2	1.0	1.5
K	na	0.0	0.0	<0.04	<0.04	na	<0.04	<0.04	<0.04	<0.04
O	1.0	2.0	11.3	13.8	5.3	8.6	8.7	16.1	4.6	7.9
Total	99.8	98.3	89.6	92.9	98.0	96.5	95.7	97.0	98.3	97.8
Me/S	1.16	1.06	1.46	2.03	1.27	1.23	1.19	1.18	1.22	1.16
Ni/(Ni+Fe)	0.56	0.21	0.91	0.24	0.46	0.38	0.43	0.46	0.47	0.43

Representative characteristics and major-element composition of sulfide in wt.%; Me/S = atomic (Cu + Fe + Ni + Co)/S; Ni/(Ni + Fe) from at.%; e: enclosed; i: interstitial; div: diverse; pn: pentlandite; gs: godlevskite; hz: heazlewoodite; cs: chalcosite; for other abbreviations, see Tables 2 and 4.

in sample K14-5b are given in Table 10 (full data set, also for xenocrysts, available online). Garnet from sheared lherzolite K14-1 has a chondrite-normalised (indicated by the subscript $_N$) REE pattern with a steep positive slope in the LREE and MREE, and unfractionated (flat) HREE (Fig. 5A). The HFSE abundances are high relative to most other garnets. Garnet from the garnet spinel lherzolite K14-3a has a pattern similar to garnet from the sheared lherzolite, with the exception of a steep negative slope between La_N and Pr_N, and higher Nb and markedly lower Ti abundance. Garnet in sample K11-6 is zoned with regard to trace elements and shows an order of magnitude difference in La_N, and smaller differences in Ce_N and Pr_N; the MREE and HREE pattern is flat at about $10 \times$ chondrite (Fig. 5B). The two other garnet harzburgites have pronounced sinusoidal REE patterns, with the hinge at $Eu_N \sim 50$ for one sample and at $Nd_N \sim 7$ for the other sample. Garnet trace-element data are available for one pyroxenite. Four of five analyses of garnet in this sample show a very steep, smooth slope between Ce_N and Lu_N and one analysis shows markedly higher La and Ce abundances and La/Ce>1 (out-

side the analytical error). $LILE_N$ and $HFSE_N$ increase almost smoothly with increasing compatibility. Apparent negative Ga anomalies are probably due to a choice of compatibility order and do not have any geological significance.

6.2. Clinopyroxene

Clinopyroxenes in the sheared lherzolite and in the garnet spinel lherzolite have similar REE patterns, starting at $La_N = 10$, peaking at slightly higher Pr_N and descending smoothly towards Lu_N (Fig. 6B). All but one clinopyroxene in spinel lherzolites have $LREE_N$ of ~ 10, a negative slope in the $MREE_N$ and flat or smoothly decreasing $HREE_N$ (Fig. 6D). One clinopyroxene has a sinusoidal REE pattern. The LREE enrichment is not accompanied by LILE or HFSE enrichment. HFSE and LILE abundances in clinopyroxenes in spinel lherzolites are similar to those in the garnet lherzolites. Clinopyroxenes in several spinel lherzolites also have low HREE abundances similar to those in garnet lherzolites. This may indicate equilibration with garnet, although garnet was not identified petrographically (Kempton et al., 1999). Clinopyroxene in a garnet-

Table 10
Representative trace-element composition of garnet, cpx and melt patch

Sample	K6-5b	S.D./1σ	K11-5	S.D./1σ	K11-6 (1)	1σ	K11-6 (2)	1σ	K14-1	S.D./1σ	K14-1
Mineral	cpx		grt		grt		grt		grt		cpx
Lithotype	pyrox		gt harz		gt harz		gt harz		gt lherz		gt lherz
n	5		5		1		1		5		5
Li	4.5	0.3	0.08	0.02	0.08	0.03	0.10	0.02	0.20	0.02	1.0
Be	0.10	0.03	<0.29		<0.05		<0.034		<0.035		0.19
B	13	2	70	10	17	1	19	1	1.3	0.2	1.5
Al	30000	1000	105000	5000	na		102924	4000	111000	4000	10500
P	40	7	120	30	120	20	118	20	130	30	32
Ca	158000	5000	46000	1000	na		37022	1000	34000	1000	125000
Sc	104	4	165	6	122	4	124	4	94	3	12.3
Ti	2400	100	400	400	2800	100	2868	100	5100	200	1280
V	350	10	440	30	300	10	278	9	270	10	200
Co	24	3	43	6	36	2	36	2	45	2	31
Ni	150	10	60	10	48	3	57	3	101	5	500
Ga	5.1	0.3	6.1	0.9	5.9	0.3	5.3	0.3	12.1	0.5	5.7
Rb	0.5	0.1	<0.2		<0.160		0.37	0.06	<0.067		0.9
Sr	83	4	<1.8		2.1	0.3	0.9	0.2	0.9	0.2	152
Y	16.0	0.7	0.8	0.3	14.5	0.5	13.0	0.5	17.4	0.6	2.4
Zr	22.3	0.8	16	10	86	3	70	3	58	2	6
Nb	0.5	0.3	1.09	0.08	0.93	0.05	0.67	0.03	0.59	0.05	0.5
Cs	<0.064		<0.10		<0.10		0.20	0.04	<0.028		<0.019
Ba	0.9	0.2	<0.15		0.47	0.07	0.09	0.03	<0.096		5
La	3.2	0.2	0.11	0.02	0.62	0.03	0.044	0.005	0.05	0.01	2.6
Ce	10.6	0.5	1.2	0.2	1.20	0.05	0.44	0.02	0.46	0.02	9
Pr	1.50	0.06	0.41	0.04	0.17	0.01	0.152	0.008	0.15	0.01	1.4
Nd	6.0	0.2	3.1	0.3	1.56	0.10	1.46	0.07	1.43	0.07	6.5
Sm	1.35	0.07	0.9	0.1	1.07	0.08	1.04	0.06	1.01	0.06	1.42
Eu	0.45	0.02	0.24	0.03	0.48	0.03	0.52	0.02	0.50	0.02	0.43
Gd	1.77	0.09	0.4	0.2	2.0	0.1	1.85	0.09	1.92	0.09	1.09
Dy	2.6	0.1	0.28	0.08	2.5	0.1	2.34	0.09	2.9	0.1	0.64
Ho	0.61	0.03	0.05	0.01	0.58	0.03	0.47	0.02	0.67	0.03	0.100
Er	1.9	0.1	0.12	0.06	1.53	0.09	1.29	0.06	1.97	0.09	0.21
Yb	1.9	0.1	0.4	0.1	1.8	0.1	1.21	0.06	2.0	0.1	0.12
Lu	0.26	0.02	0.08	0.02	0.27	0.02	0.22	0.01	0.32	0.02	0.013
Hf	0.93	0.07	0.71	0.08	2.4	0.1	1.38	0.07	1.45	0.09	0.35
Ta	0.017	0.005	0.08	0.02	0.039	0.009	0.036	0.005	0.036	0.005	0.02
Pb	4.1	0.5	0.19	0.04	<0.125		0.13	0.05	<0.205		0.3
Th	0.16	0.04	0.08	0.03	0.041	0.009	0.012	0.003	0.015	0.003	0.06
U	0.03	0.01	0.09	0.04	0.017	0.007	0.018	0.003	0.025	0.005	0.01

Representative trace-element abundances of garnet and clinopyroxene in xenoliths in ppm; S.D.: standard deviation (in italics); 1σ: one sigma error (reflecting the within-run precision); where multiple analyses were performed, standard deviation is presented (in italics) if it was greater than 1σ; for other abbreviations, see Tables 2 and 4.

bearing pyroxenite has La_N to Gd_N of ~ 3–5, which decreases smoothly toward $Lu_N = 0.5$. Clinopyroxene in a garnet-free pyroxenite has an almost flat REE pattern with all abundances at 8–20 × chondritic. HREE and most LILE and HFSE abundances are higher in clinopyroxenes from the garnet-free pyroxenite.

7. Geothermobarometry

Different geothermobarometers were applied to mantle xenoliths from Buffalo Hills kimberlites, depending on metamorphic facies and assemblage (see Table 11). For exsolution-free spinel lherzolites, temperature estimates range from 823 and 1152 °C

(mean 946 °C), using $T_{Ca-in-orthopyroxene}$ of Brey and Köhler (1990) and between 787 and 847 °C (mean 826 °C; at a nominal pressure of 30 kbar), using T_{WES91} of Witt-Eickschen and Seck (1991). Temperatures and pressures were solved simultaneously for the garnet spinel lherzolite and the sheared garnet lherzolite, using $T_{Ca-in-orthopyroxene}$ and P_{NG} of Nickel and Green (1985). The garnet spinel lherzolite gives a $T_{Ca-in-orthopyroxene}$ of 851 °C and P_{NG} of 27 kbar, while the sheared garnet lherzolite gives $T_{Ca-in-ortho-pyroxene}$ of 1270 °C and P_{NG} of 58 kbar. Temperature estimates for the three inferred garnet harzburgites vary between 890 and 1126 °C (at a nominal pressure of 50 kbar, using T_{OW79}). Temperatures and pressures were solved simultaneously for three garnet pyroxenites: temperatures vary between 729

Table 10 (continued)

Sample Mineral Lithotype n	S.D./1σ	K14-3a grt gt sp lherz 7	S.D./1σ	K14-3a cpx gt sp lherz 5	S.D./1σ	K14-5b 5 sp lherz 5	S.D./1σ	K14-5b melt 5	S.D./1σ	K14-6 cpx sp lherz 5	S.D./1σ	K14-7 cpx sp lherz 6	S.D./1σ
Li	0.2	0.26	0.05	0.8	0.2	0.8	0.4	2.2	0.9	1.3	0.2	1.0	0.2
Be	0.02	<0.043		0.06	0.02	0.04	0.02	0.13	0.02	0.04	0.01	0.08	0.02
B	1.0	1.0	0.4	1.5	0.7	1.3	0.9	90	30	23	2	25	2
Al	400	131000	7000	14000	3000	17000	1000	3500	100	15600	700	17400	900
P	7	44	9	30	20	21	4	30	20	18	3	20	4
Ca	4000	42000	1000	169000	5000	169000	5000	2100	700	170000	5000	169000	5000
Sc	0.4	140	10	30	1	79	8	3.7	0.2	51	2	41	1
Ti	60	900	200	800	100	430	10	170	10	300	10	1020	50
V	10	160	30	180	30	200	10	27	5	200	10	240	10
Co	3	37	4	23	2	25	3	300	300	19	3	15	2
Ni	40	7	1	260	30	280	40	<10000		310	30	230	20
Ga	0.5	3.7	0.4	4.6	0.5	1.9	0.2	1.6	0.2	1.5	0.1	2.6	0.2
Rb	0.6	<0.07		0.6	0.3	0.2	0.1	11	2	0.4	0.4	2	1
Sr	6	0.4	0.2	176	30	135	4	210	50	77	2	63	2
Y	0.1	24	2	0.9	0.1	2.4	0.1	0.23	0.02	1.60	0.06	1.7	0.1
Zr	2	36	10	5.2	0.6	9.2	0.5	7	2	8.0	0.3	12.3	0.4
Nb	0.5	2.2	1.0	1.9	0.9	0.12	0.03	9	3	0.39	0.06	0.4	0.1
Cs	<0.031			0.04	0.01	<0.04		0.22	0.05	0.13	0.02	<0.08	
Ba	6	0.2	0.1	40	20	6	2	28	7	1.5	0.7	7	4
La	0.5	0.3	0.5	3	1	2.16	0.07	2	1	2.6	0.1	2.0	0.1
Ce	1	0.4	0.4	8	2	5.9	0.2	4	3	7.7	0.5	7.1	0.3
Pr	0.1	0.04	0.01	1.14	0.18	0.74	0.05	0.3	0.2	1.13	0.04	1.14	0.06
Nd	0.4	0.39	0.09	4.87	0.69	3.2	0.1	0.8	0.5	4.8	0.2	5.1	0.3
Sm	0.07	0.5	0.1	0.89	0.12	0.66	0.05	0.10	0.05	0.84	0.04	1.07	0.06
Eu	0.03	0.30	0.02	0.2	0.0	0.20	0.01	0.03	0.01	0.22	0.01	0.28	0.01
Gd	0.06	1.59	0.09	0.6	0.1	0.59	0.06	0.06	0.02	0.57	0.03	0.82	0.05
Dy	0.04	3.6	0.3	0.29	0.03	0.48	0.04	0.03	0.01	0.36	0.02	0.47	0.07
Ho	0.006	1.0	0.1	0.036	0.008	0.09	0.01	0.008	0.003	0.065	0.004	0.07	0.01
Er	0.01	3.2	0.6	0.06	0.01	0.25	0.02	0.02	0.01	0.15	0.02	0.14	0.03
Yb	0.02	3.9	0.9	<0.02		0.27	0.06	0.02	0.01	0.13	0.02	0.07	0.01
Lu	0.004	0.7	0.2	0.003	0.001	0.048	0.005	0.004	0.002	0.020	0.003	0.008	0.002
Hf	0.03	0.8	0.2	0.33	0.03	0.35	0.03	0.15	0.03	0.29	0.02	0.69	0.05
Ta	0.02	0.019	0.007	0.03	0.02	0.019	0.005	0.28	0.09	0.049	0.007	0.051	0.006
Pb	0.2	<0.23		1.3	0.2	0.3	0.1	0.7	0.6	0.5	0.2	0.7	0.4
Th	0.05	0.03	0.02	0.2	0.2	0.06	0.02	0.12	0.09	0.10	0.03	0.08	0.03
U	0.01	0.05	0.05	0.03	0.02	0.016	0.003	0.4	0.1	0.026	0.005	0.02	0.02

and 793 °C (using $T_{Ca-in-orthopyroxene}$) and pressures vary between 12 and 13 kbar (using P_{NG}). The temperature and pressure estimate for one clinopyroxene-free garnet pyroxenite is 628 °C and 9 kbar, respectively (when T_{Harley} of Harley, 1984, is solved simultaneously with P_{NG}). The temperature estimate for two garnet-free pyroxenites is 742 and 750 °C (using $T_{Ca-in-orthopyroxene}$ at a nominal pressure of 15 kbar) and for two orthopyroxene-free garnet pyroxenites, it is 713 and 906 °C (using T_{Krogh} of Krogh, 1988).

Ni-in-garnet thermometry was applied to garnet xenocrysts (Griffin et al., 2004) classified as garnet from garnet spinel lherzolite, wehrlite, lherzolite and Ca-harzburgite based on their Cr–Ca relationships. Garnets from garnet spinel lherzolites give temperatures from 660 to 690 °C (mean 670 °C), wehrlite garnets from 710 to 1040 °C (mean 790 °C), lherzolite garnets from 610 to 1340 °C (mean 940 °C) and Ca-harzburgite garnets from 710 to 1200 °C (mean 1060 °C). Garnets from garnet spinel lherzolites give minimum pressures ($P_{Cr-in-gt}$; Ryan et al., 1996) from 19 to 21 kbar (mean 20 kbar, $n = 3$), wehrlite garnets from 11 to 46 kbar (mean 29 kbar, $n = 13$), lherzolite garnets from 24 to 55 kbar (mean 49 kbar, $n = 127$) and Ca-harzburgite garnets from 24 to 55 kbar ($n = 9$).

Application of $P_{Cr-in-grt}$ presupposes equilibrium with chromite and application of this method in the absence of chromite results in a minimum pressure; with a large enough database, the envelope of maximum pressures at a given temperature defines the
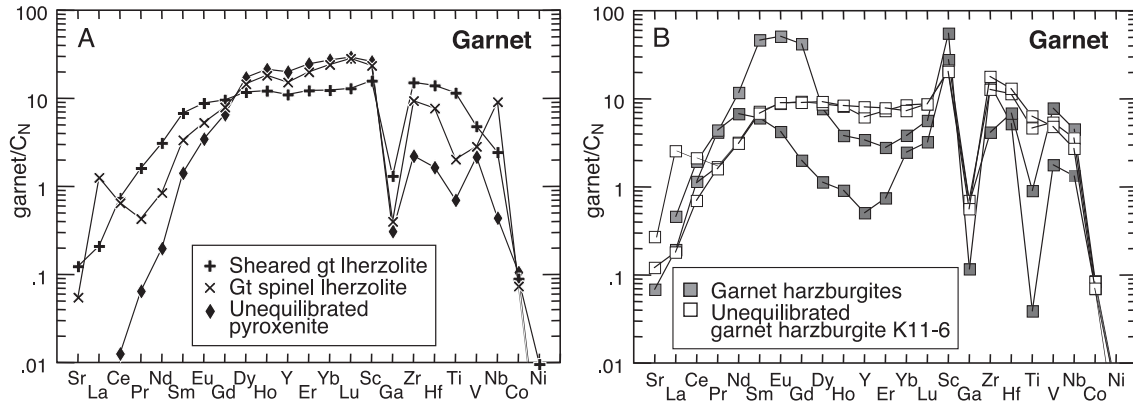
Fig. 5. Extended trace-element patterns in garnet. C_N denotes normalisation to chondrite of McDonough and Sun (1995).
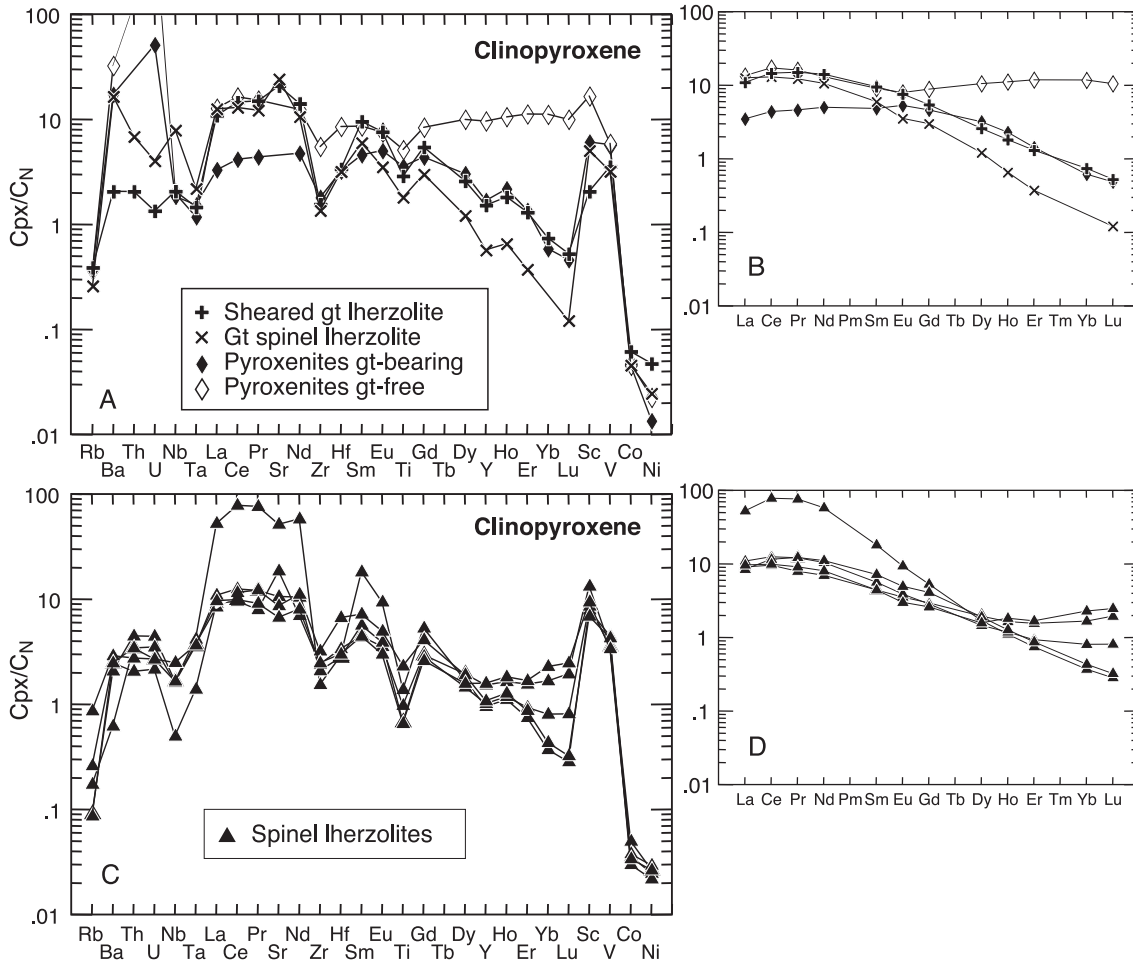

Fig. 6. Extended trace-element patterns (A and C) and REE patterns (B and D) in cpx. C_N denotes normalisation to chondrite of McDonough and Sun (1995).

geotherm (Ryan et al., 1996). For the mantle beneath the BHT, a geotherm of 38–39 mW/m^2 is obtained (Fig. 7). The sheared lherzolite gives a very high temperature and the highest pressure of all samples, consistent with its microstructure and enrichment in basaltic components, which is similar to high-temperature sheared peridotites interpreted to have been infiltrated by asthenospheric melts shortly before entrainment in the kimberlite (Smith and Boyd, 1987; Griffin et al., 1987). Together with several harzburgitic garnet xenocrysts, it may define a kink in the geotherm. The garnet spinel lherzolite and pyroxenites plot off the geotherm, possibly due to major-element disequilibrium caused by sluggish reaction rates in the cool shallow lithosphere. Another group of xenocrysts gives low temperatures for their pressures (grey field in Fig. 7). The cause for this is not known.

8. Whole-rock reconstruction

Whole rocks were reconstructed by combining modal abundance data (obtained by counting on average >1000 points) and mineral analyses (data available online). Garnet peridotites with assumed altered orthopyroxene were reconstructed using the relationship between olivine MgO and FeO^t contents and orthopyroxene MgO, FeO and SiO$_2$ contents in 55 garnet peridotites from Lac de Gras (Pearson et al., 1999 and unpublished data) and average contents of other major elements in orthopyroxene (orthopyroxene MgO = 0.66∗ol MgO + 2.12, r^2 = 0.84; orthopyroxene FeO = 0.511∗ol FeO = 0.73, r^2 = 0.89; orthopyroxene SiO$_2$ = 0.495∗ol MgO + 32.6, r^2 = 0.31). Reconstructed whole rocks will be used to estimate the degree of partial melting they have experienced. Uncertainties in mineral modes from medium- to coarse-grained samples are estimated to be about 10% (Jerde et al., 1993). Because the grain sizes of most xenolith samples from the Buffalo Hills kimberlites are small compared to the size of the thin sections, the actual error may be closer to 5%.

9. Sr–Nd–Hf isotope data

Sr, Nd and Hf isotope data were obtained for garnet in two garnet harzburgites, garnet and clinopyroxene in the sheared garnet lherzolite, garnet in the garnet spinel peridotite and clinopyroxene in one garnet pyroxenite and in two spinel peridotites (Table 12). The terms unradiogenic and radiogenic refer to isotopic compositions relative to a chondritic reservoir (CHUR) at the time of kimberlite eruption (ca. 85 Ma ago). ε_{Hf} and ε_{Nd} indicate the parts per 10,000 deviation of the isotopic composition of the sample from that of a model chondritic source. Model ages are calculated relative to a model depleted mantle source (T_{DM}).

Mineral separation of harzburgite K11-3 revealed the presence of two garnet populations, of which one is purple and transparent, with smooth shiny surfaces and one is red and opaque, with a dull surface. Their Nd and Hf isotope ratios are almost indistinguishable but different from all other separates measured and confirm that these two separates were derived from a single sample and are not due to contamination. Garnets in both garnet harzburgites (K11-3 and K11-5) have similar ^{143}Nd/^{144}Nd around the chondritic value at the time of kimberlite eruption (ε_{Nd} = − 1.2 to 0.0) and radiogenic ^{176}Hf/^{177}Hf (ε_{Hf} = 16.3 to 37.0). Sm–Nd T_{DM} are negative for K11-3 and at least Proterozoic for K11-5; Lu–Hf T_{DM} are Proterozoic for K11-3 and implausible for K11-5.

The garnet in K14-1 has relatively low ε_{Hf} (10.1) and ε_{Nd} (4.2), whereas the clinopyroxene has identical Nd (within the uncertainty) but radiogenic Hf (ε_{Hf} = 63.4). Garnet and clinopyroxene yield an internal Sm–Nd isochron age of 86 ± 17 Ma, similar to the kimberlite eruption age. However, the Lu–Hf isochron age is negative, indicating isotopic disequilibrium. Sr in the clinopyroxene is unradiogenic (^{87}Sr/^{86}Sr$_{measured}$ = 0.703546). Garnet from garnet spinel lherzolite K14-3 has radiogenic Hf and Nd (ε_{Hf} > 80, ε_{Nd} > 50); not enough clinopyroxene could be separated for isotope analysis.

Clinopyroxenes in two spinel lherzolites have unradiogenic Nd and Sr (ε_{Nd} = − 16.7 and − 8.9, respectively, ^{87}Sr/^{86}Sr$_{measured}$ = 0.703997 and 0.703727, respectively) and yield Early Proterozoic T_{DM}. Clinopyroxenes in K14-6 have radiogenic Hf and a young model age (ε_{Hf} = 18.3; 27 Ma). Clinopyroxenes in K14-7 have unradiogenic Hf (ε_{Hf} = − 11.1; T_{DM} = 1.2 Ga). Garnet in the pyroxenite has radiogenic Nd and unradiogenic Hf (ε_{Nd} = 10.3;

Table 11
Temperature–pressure estimates

Sample	Lithotype	Paragenesis used	T_{BKN}	$T_{Ca\text{-}in\text{-}opx}$	T_{EG}	T_{Krogh}	T_{OW79}	T_{Harley}	T_{WES91}	$T_{Ni\text{-}in\text{-}grt}$
K6-1	sp lherz	ol, opx, cpx	810	1001					833	
K6-2a	sp lherz	ol, opx, cpx core	699	1012					844	
K6-2a	sp lherz	ol, opx, cpx rim	590	1012					844	
K6-2b	sp lherz	ol + cpx core, opx	718	991					847	
K6-2b	sp lherz	ol + cpx rim, opx	686	991					847	
K6-2b2	gt pyrox	gt, opx core						657		
K6-2b2	gt pyrox	gt, opx rim						646		
K6-3	sp lherz	ol, opx, cpx	744	866					818	
K6-4	sp lherz	ol, opx, cpx core	818	888					825	
K6-4	sp lherz	ol, opx, cpx rim	944	888					825	
K6-5a	sp lherz	ol, opx, cpx	712	1152					845	
K6-5b	pyrox	opx, cpx	742	750					919	
K11-3	gt harz	ol, gt					890			755
K11-5	gt harz	ol, Ca-poor gt					1126			1093
K11-6	gt harz	ol rim, gt core					1096			1080
K11-6	gt harz	ol rim, gt rim					1060			1080
K14-1	gt lherz	ol, opx, cpx, gt	1288	1233	1267	1236	1194	1142	787	1303
K14-2a	gt pyrox	gt, opx, cpx core	757	736	792	705		705	754	616
K14-2a	gt pyrox	gt, opx, cpx rim	682	736	758	669		705	754	
K14-2ba	sp lherz	ol, opx, cpx	590	938					811	
K14-2bb	gt pyrox	gt opx, cpx core	575	753	753	670		678	797	
K14-2bb	gt pyrox	gt opx, cpx rim	535	753	735	650		678	797	
K14-2c	sp lherz	ol, opx + cpx core	725	1011					838	
K14-2c	sp lherz	ol, opx + cpx rim	743	925					815	
K14-3a	gt lherz	ol, opx, cpx, gt	765	817	822	749	742	842	747	
K14-3c	gt pyrox	gt cpx			791	713				
K14-4a	sp lherz	ol + opx, cpx core	524	926					823	
K14-4a	sp lherz	ol + opx, cpx rim	892	926					823	
K14-4b	gt pyrox	Ca-poor cpx, gt			969	906				
K14-5a	sp lherz	ol, opx		947					839	
K14-5b	sp lherz	ol, opx, cpx	355	862					787	
K14-5c	gt pyrox	gt, cpx domain 5			848	758				
K14-5c	gt pyrox	gt, cpx domain 4			767	684				
K14-5c	gt pyrox	gt, opx domain 2		742				674	750	
K14-5c2	pyrox	opx cpx	716	742					929	
K14-5d	sp lherz	ol, opx, cpx	273	823					833	
K14-5f	gt pyrox	gt, opx + cpx core	539	801	853	785		716	842	
K14-5f	gt pyrox	gt, opx + cpx rim	588	765	789	715		681	815	
K14-6	sp lherz	ol, opx, cpx	638	928					812	
K14-7a	sp lherz	ol, opx, cpx core	435	872					795	
K14-7a	sp lherz	ol, opx, cpx rim	801	872					795	
K14-8	sp lherz	ol, opx + cpx core	491	976					840	
K14-8	sp lherz	ol, opx + cpx rim	790	915					822	

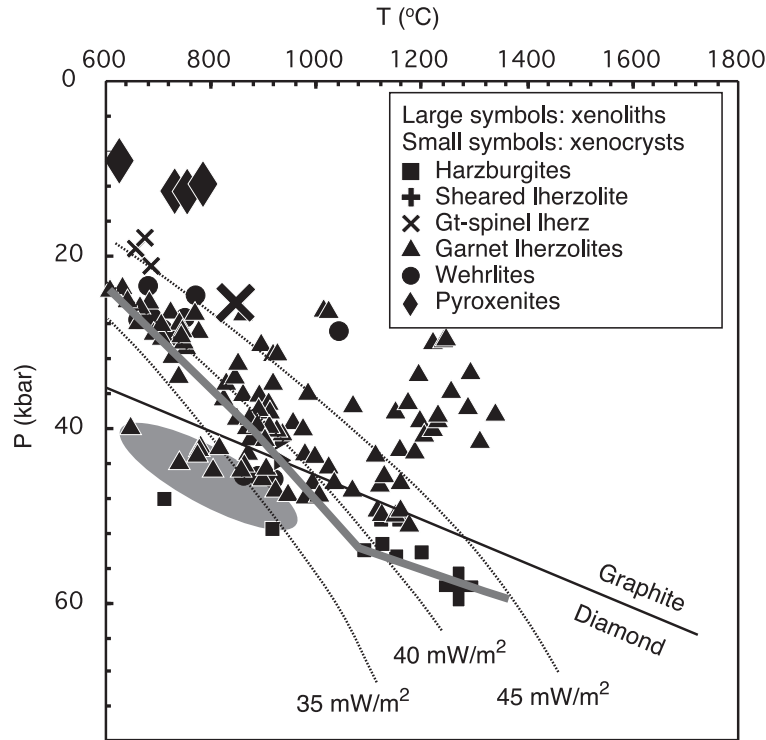| Sample			$T_{Ca\text{-}in\text{-}opx}$ at P_{NG}	P_{NG} at $T_{Ca\text{-}in\text{-}opx}$	T_{Harley} at P_{NG}	P_{NG} at T_{Harley}	T_{BKN} at P_{NG}	P_{NG} at T_{BKN}		
K6-2b2	gt pyrox	gt, opx core			628	9				
K14-1	gt lherz	ol, opx, cpx, gt	1270	58	1167	54	1311	60		
K14-2a	gt pyrox	gt, opx, cpx core	729	13	685	11	673	10		
K14-2bb	gt pyrox	gt opx, cpx core	746	13	649	9	552	5		
K14-3a	gt sp lherz	ol, opx, cpx, gt	851	27	746	22	737	21		
K14-5f	gt pyrox	gt, opx + cpx core	793	12	679	8	522	2		

Fig. 7. Simultaneously solved pressure and temperature for garnet xenocrysts, garnet lherzolites and garnet pyroxenites, as discussed in the text. The highest pressures at a given temperature for garnet geothermobarometry define the local geotherm (thick grey line). Sheared lherzolite K14-1 forms part of an inflected array. Graphite–diamond phase boundary of Kennedy and Kennedy (1976); model geotherms after Pollack and Chapman (1977).

$\varepsilon_{Hf} = -2.3$) and yields a Proterozoic model age for both isotope systems.

10. Re–Os isotope systematics of sulfides

Re–Os isotope data were obtained for one sulfide enclosed in orthopyroxene and five interstitial sulfides in six peridotites. $^{187}Re/^{188}Os$ ratios range from 0.0938 ± 0.0024 to 10.71 ± 0.38. $^{187}Os/^{188}Os$ ratios range from 0.1172 ± 0.0026 to 2.4000 ± 0.0051, corresponding to positive, i.e., suprachondritic, γ_{Os} for four of the samples and negative (subchondritic)

γ_{Os} for two of the samples (Table 13; γ_{Os} is percent deviation from $^{187}Os/^{188}Os$ of a model chondritic source). These latter give Re-depletion ages (T_{RD} as defined by Walker et al., 1989) of 0.40 ± 0.18 and 1.46 ± 0.38 Ga. Sulfide in the melt patch in sample K14-5b is one of the samples with suprachondritic $^{187}Os/^{188}Os$ and gives a model age of 1.73 ± 0.13 Ga. This sample has $^{187}Re/^{188}Os > 10$, requiring large corrections for the overlap of ^{187}Re on ^{187}Os and its $^{187}Os/^{188}Os$ probably has a larger uncertainty than indicated by the internal error. In addition, a second analysis of sulfide in this sample has revealed significant heterogeneity of $^{187}Os/^{188}Os$. The sample giving

Table 12
Sr, Nd and Hf isotope ratios and model ages for garnet and cpx (solution analyses)

Sample	Type	$^{87}Sr/$$^{86}Sr$	2 S.E.	$^{147}Sm/$$^{144}Nd$ [a]	$^{143}Nd/$$^{144}Nd$	2 S.E.	$\varepsilon_{Nd(T)}$ [b]	T_{DM} [c]	$^{176}Lu/$$^{177}Hf$ [a]	$^{176}Hf/$$^{177}Hf$	2 S.E.	$\varepsilon_{Hf(T)}$ [b]	T_{DM} [c]
K11-3 purple gt	gt harz	na	na	0.796	0.512780	0.000010	−1.2	−193	0.036	0.283239	0.000011	16.3	1677
K11-3 red gt	gt harz	na	na	0.796	0.512844	0.000026	0.0	−176	0.036	0.283268	0.000024	17.4	981
K11-5 gt	gt harz	na	na	0.180	0.512476	0.000010	−0.5	3178	0.016	0.283766	0.000019	36.1	−1192
K11-5 gt repeat	gt harz	na	na	0.180	0.512495	0.000014	−0.1	3094	0.005	0.283791	0.000011	37.0	−1252
K14-1 cp	sheared gt lherz	0.703546	0.000024	0.137	0.512698	0.000007	4.3	901	0.031	0.284519	0.000132	63.4	−2066
K14-1 gt	sheared gt lherz	na	na	0.443	0.512862	0.000012	4.2	−305	0.031	0.283055	0.000011	10.1	1681
K14-1 gt repeat	sheared gt lherz	na	na	0.443	0.512877	0.000020	4.5	−295	0.119	0.283034	0.000004	9.4	1824
K14-3 gt	gt–sp lherz	na	na	0.838	0.515460	0.000013	50.6	469	0.119	0.285434	0.000009	89.3	1310
K14-3 gt repeat	gt–sp lherz	na	na	0.838	0.515443	0.000010	50.3	465	0.005	0.285272	0.000010	83.6	1203
K14-5f cp	gt pyrox	0.703721	0.000012	0.201	0.513038	0.000008	10.3	1785	0.010	0.282661	0.000015	−2.3	936
K14-6 cp	sp lherz	0.703997	0.000022	0.110	0.511606	0.000011	−16.7	2246	0.002	0.283251	0.000079	18.3	27
K14-7 cp	sp lherz	0.703727	0.000022	0.131	0.511982	0.000008	−8.9	2097		0.282407	0.000031	−11.1	1213

Sr–Nd–Hf isotope data for solutions of clinopyroxene and garnet separates.

[a] Calculated from LA–ICPMS trace-element analyses and isotopic abundances of Sm and Nd and arbitrarily quoted to three significant figures.

[b] Parts per 10,000 deviation from chondrite (values of Wasserburg et al., 1981; Blichert-Toft and Albarède, 1997, respectively) at the time of kimberlite eruption ca. 85 Ma ago.

[c] Depleted mantle source (DM) of DePaolo (1981) and Griffin et al. (2000), respectively.

a 1.46 Ga T_{RD} has a model age of 1.89 ± 0.38 Ga. Future and implausibly old model ages suggest disturbance of the Re–Os budget by secondary Re-addition and/or ^{187}Os-addition.

11. Discussion

11.1. Lithosphere structure and lithosphere–asthenosphere boundary (LAB)

A preliminary stratigraphy of the SCLM beneath the BHT has been derived by comparing the relative abundances of peridotite classes (based on major- and trace-element abundances in garnet xenocrysts) and Mg-numbers in olivine in different depth or temperature intervals, respectively (Griffin et al., 2004; Fig. 8A–C). Xenolith types (this study) provide a cross-check (Fig. 8D). Fertile garnet lherzolites are concentrated at shallow depths (<140 km) and prevail at depths <110 km; depleted peridotites are concentrated between ca. 120 and 160 km and prevail between ca. 130 and 150 km; melt-metasomatised lherzolites, similar to sheared lherzolites (Griffin et al., 2003), are concentrated between ca. 140 and 180 km and prevail at depths >170 km; a relatively steady proportion of depleted metasomatised peridotites occurs between ca. 110 and 180 km depth (Fig. 8A). Mg-numbers in olivine, derived by inversion of the garnet–olivine thermometer of O'Neill and Wood (1979) (Gaul et al., 2000), are relatively steady between 90 and 140 km depth at 92.0–92.2% and decrease toward 90.3% at ∼ 180 km depth (Fig. 8B). This is consistent with the increasing proportion of melt-metasomatised peridotites in this depth interval. Data for the xenoliths agree well with the xenocryst-derived stratigraphy, as pyroxenite and garnet spinel lherzolite are restricted to the shallow mantle and harzburgite with Ca-saturated garnet is concentrated in a layer between ∼ 140 and 160 km (∼ 1000–1200 °C; Fig. 8C,D; Table 14).

Temperatures for spinel lherzolites were calculated using the Ca-in-orthopyroxene thermometer of Brey and Köhler (1990) and the formulation of Witt-Eickschen and Seck (1991), both of which tend to overestimate for temperatures <900 °C (Smith, 1999). This may explain their apparent persistence to temperatures above the spinel–garnet transition, which is

Table 13
Re–Os isotope composition of sulfide (in situ analyses)

Sample	K6-1-2	K14-3a	K14-5b-1	K14-5b-2	K14-5d-1	K14-6	K14-7a-1
$^{187}Re/^{188}Os$	0.540	0.513	10.71	9.777	0.0938	1.220	0.5471
2 S.E.	0.024	0.026	0.38		0.0024	0.032	0.0048
$^{187}Os/^{188}Os$	0.1679	0.1809	0.4298	1.016	0.1172	2.4000	0.1244
2 S.E.	0.0012	0.0027	0.0160	0.018	0.0026	0.0051	0.0012
γOs	32.19	42.4	240	700	− 7.7	1789	− 2.12
2 S.E.	0.94	2.1	10	10	2.1	4	0.96
T_{RD} [Ma]	na	na	na	na	1455	na	402
+/ −					381		182
T_{CHUR} [Ma]	15 492	23 549	1737	5437	1893	79 707	− 1114
+/ −	2808	4832	132	371	378	7811	114

Re–Os isotope data from in situ analysis of sulfides; γOs is the percent deviation from chondritic $^{187}Os/^{188}Os$; T_{RD} is rhenium depletion age (Walker et al., 1989), T_{CHUR} is derived by referral to chondrite Os isotopic evolution (chondrite of Walker et al., 1994).

constrained by garnet spinel lherzolite. The relatively Cr-rich nature of the spinel peridotites may also act to delay the stabilisation of garnet (Webb and Wood, 1986). The absence of nonsheared garnet lherzolites in the xenolith suite contrasts with the abundance of lherzolitic garnet xenocrysts and may indicate that this rock type was preferentially comminuted during entrainment in the kimberlite. The possibility that the sheared lherzolite defines an inflection of the 38–39 mW/m^2 geotherm, combined with its microstructure

and enrichment in basaltic components, suggests that it was derived from close to the lithosphere–asthenosphere boundary (Smith and Boyd, 1987). It constrains the depth of the SCLM beneath the BHT to somewhere in the vicinity of 180 km.

11.2. Melting

The degree of depletion can be assessed by comparison of whole rocks, reconstructed from min-
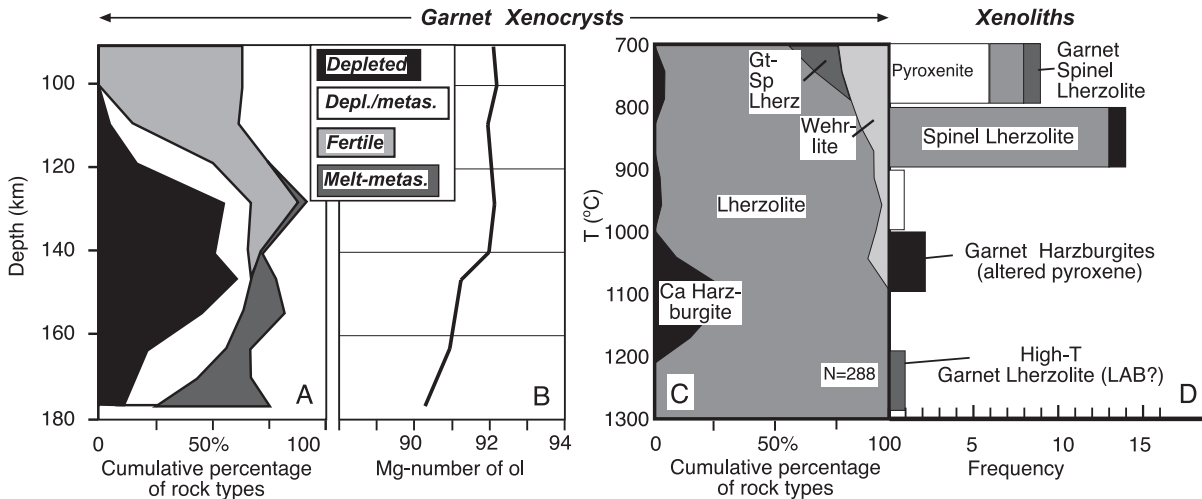

Fig. 8. Lithosphere structure beneath the BHT from (A) garnet classes against depth (derived by multivariate analyses of trace-element abundances in garnet xenocrysts (Griffin et al., 2002) and Ni-in-garnet thermometry (Ryan et al., 1996)); (B) Mg-number in olivine against depth (converted from major-element composition of garnet xenocrysts using the formulation of Gaul et al., 2000); (C) garnet classes against temperature (using Cr_2O_3–CaO relationships of garnet xenocrysts); (D) xenolith lithologies plotted against temperatures (different geothermometers were used, according to assemblage and metamorphic facies of the sample, as outlined in the text). Sections (A) to (C) from Griffin et al. (2004).

eral compositions weighted by modes, with experimental melting residues (Fig. 9A,B). Keeping in mind that the accuracy of such estimates is limited by the uncertainties in the modal analyses, most samples from the BHT have FeO–SiO$_2$ and FeO–MgO relationships consistent with a loss of between 20–40% partial melt at pressures between 1 and 4 GPa, assuming a fertile peridotite starting composition (Walter, 1999). Two of the garnet harzburgites appear to have been depleted more strongly, at pressures up to 7 GPa. The sheared garnet lherzolite and garnet spinel lherzolite are too FeO-rich to represent samples depleted by an extraction of melt and plot outside the scale chosen in Fig. 9. Three samples lie on a trend to high SiO$_2$, indicating high orthopyroxene/olivine similar to peridotites from Kaapvaal and to a lesser extent Siberia, although displaced toward higher SiO$_2$ for a given FeO content (Fig. 9C).

11.3. Old metasomatism

Cryptic metasomatism is evidenced by incompatible element enrichment in garnet and clinopyroxene in otherwise depleted samples from Buffalo Hills, both in the shallow mantle (spinel stability field) and in the deep mantle (garnet stability field). Most of these samples have well-equilibrated microstructures, and homogeneous garnet and clinopyroxene compositions with regard to major and trace elements, suggesting that the enrichment predates entrainment in the host kimberlite.

Zr–Y relationships can be used to distinguish garnets from different sources: fertile, depleted and melt-metasomatised. In addition, sources that were metasomatised by a silicate melt can be distinguished from sources that were metasomatised by a distinct metasomatic agent associated with phlogopite-bearing peridotite (''phlogopite'' metasomatism; Griffin

Table 14
Average trace-element composition of garnet xenocrysts

Sample	Fertile lherz	Depl lherz	Sili metas lherz	Phlog metas lherz	Fertile harz	Depl harz	Fertile gt sp lherz	Depl gt sp lherz	Sili metas gt sp lh	Fertile wehr	Depl wehr
n	4	40	29	19	2	7	10	4	3	9	4
Ni	18	39	65	34	24	68	15	16	12	14	36
Co	34	36	44	37	42	38	38	37	39	35	36
V	150	290	250	240	200	320	130	100	130	160	410
Sc	170	160	120	180	230	210	200	160	160	220	180
Ti	680	430	2600	420	500	850	370	35	440	430	340
Y	33	3.2	17	5.2	24	3.4	22	5.20	21	30	2.5
Ce	0.59	1.3	1.8	0.85	na	1.7	1.2	0.45	3.0	1.2	2.8
Nd	1.9	3.5	2.4	3.0	na	4.6	1.6	2.3	1.8	1.8	3.7
Sm	1.3	1.5	1.4	2.2	na	1.4	1.1	1.75	1.4	1.3	1.4
Eu		0.45	0.64	0.90	0.87	0.49	0.51	0.64	0.77	0.77	na
Gd	2.0	1.07	2.51	2.5	1.9	1.1	1.9	1.6	1.9	1.9	1.6
Dy	5.2	0.88	3.1	1.61	4.5	1.5	3.5	0.98	3.3	4.2	na
Ho	1.1	0.18	0.73	0.32	1.4	0.33	0.82	0.18	0.92	1.1	na
Er	3.8	0.64	2.0	0.65	3.7	0.91	2.4	0.65	2.6	4.0	1.1
Yb	4.0	0.90	2.2	0.79	2.9	0.89	3.0	0.84	3.2	4.8	1.4
Nb	0.33	1.1	0.68	0.69	na	2.1	0.41	0.37	0.90	0.68	0.85
Zr	15	14	54	57	21	13	15	16	34	20	12
Hf	0.55	0.63	1.2	0.92	na	0.80	0.54	0.34	0.83	0.84	na
Sr	2.0	2.3	1.4	0.57	na	3.1	0.74	0.26	6.4	1.5	1.6
Ga	5.2	5.8	10	4.4	11	7.0	2.9	2.2	5.3	3.7	6.8
T_{Ni}	774	957	1121	919	827	1140	737	747	696	716	933

Average trace-element abundances of garnet xenocrysts (analyses of Griffin et al., 2004) in ppm; the basis for the classification is the Cr–Ca relationship combined with trace-element relationships explained in the Discussion; abundances are arbitrarily given to two significant figures; Ni-in-garnet thermometer ($T_{\text{Ni-in-grt}}$) of Ryan et al. (1996); for abbreviations, see Tables 2 and 3.
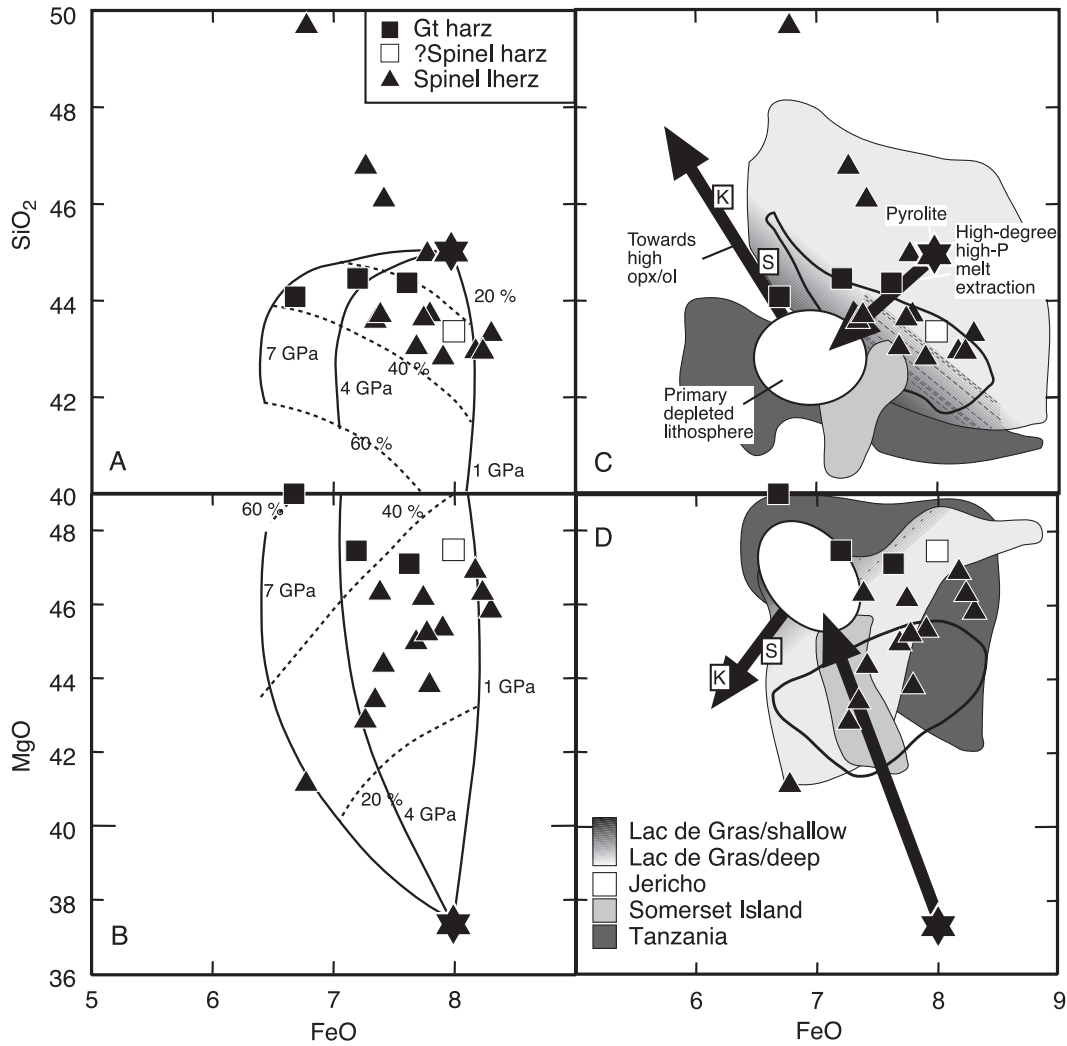
Fig. 9. Whole-rock FeO against (A) SiO_2 and (B) MgO of peridotites from the Buffalo Hills kimberlites (reconstructed from mineral data and modal estimates). (A) and (B) compared to experimental residues of isobaric batch melting at different pressures (solid lines, pressures in GPa) of pyrolite (star) for different degrees of partial melting (hatchured lines, percentages; from Walter, 1999); (C, D) partial melting trend, primary depleted lithosphere, trend towards high opx/ol ratios and average compositions of peridotites from the Kaapvaal craton (K) and Siberia (S) (from Walter, 1999); also shown are fields for peridotites from Lac de Gras (central Slave craton: Pearson et al., 1999; unpublished data), Jericho (north-central Slave craton: Kopylova et al., 1999), Somerset Island (Schmidberger and Francis, 1999) and Tanzania (Lee and Rudnick, 1999).

et al., 1999c; Fig. 10A). Garnet from the high-temperature sheared lherzolite, from the garnet spinel lherzolite and from the garnet harzburgite that has a nonsinusoidal REE pattern (see Fig. 5B) plot in the silicate melt metasomatism field. Garnets in the two garnet harzburgites with sinusoidal REE patterns plot in the depleted field and between the melt and "phlogopite" metasomatism field, respectively. Most

garnet xenocrysts plot in the depleted or silicate melt-metasomatised field; only a few garnet xeno-crysts have Zr–Y relationships indicative of fertile peridotite.

Xenocrysts were grouped according to their lithologies ($CaO–Cr_2O_3$ relationships) and Zr–Y relationships shown in Fig. 10A, and average compositions were calculated. A comparison of their

averaged chondrite-normalised REE patterns (Fig. 11) shows that garnets in fertile lherzolites and garnet spinel lherzolites have smoothly increasing REE_N abundances from Ce_N to Lu_N. In both lithologies, silicate melt metasomatism produces garnets with REE_N patterns similar to fertile peridotites, with the exception of a small increase ($2-3 \times$ chondrite) in the most incompatible LREE, and an additional positive Eu anomaly in garnet from the garnet spinel lherzolite. Strikingly, garnets in all depleted peridotite types have sinusoidal REE_N patterns with a hinge at Sm_N. "Phlogopite" metasomatism also produced a sinusoidal REE_N pattern, with a hinge at Eu_N. $HREE_N$ in depleted types are three to five times lower than in corresponding undepleted types, and this is evident also in their low Sc/Y. REE data for harzburgitic xenocrysts are incomplete, and their patterns are not shown. Some of the averaged REE patterns of the garnet xenocrysts show positive Eu anomalies. By contrast, garnets in analysed xenoliths do not show Eu anomalies.

In order to further distinguish between different styles of metasomatism and to identify the cause of sinusoidal REE patterns in otherwise depleted peridotites, the $Zr/Sm-Ce/Yb$ relationships in garnets were investigated. Interaction with silicate melt tends to increase HFSE, which are more incompatible and therefore enriched in melts, relative to MREE, which are less incompatible (i.e., bulk distribution coefficients controlled by garnet/melt and clinopyroxene/melt are higher for Sm and Eu than for Zr and Ti; e.g., Hauri et al., 1994). By contrast, increased LREE/HREE at restricted HFSE/MREE ratios are diagnostic of interaction with carbonatite melts, and these relationships may be used to distinguish carbonatite from silicate melt metasomatism (Rudnick et al., 1993; Klemme et al., 1995; Ionov, 1998; Coltorti et al., 1999, 2000).

In a plot of Zr/Sm_N against Ce/Yb_N in garnet, many lherzolitic garnets that are identified as silicate melt-metasomatised in the $Zr-Y$ diagram show evidence for enrichment in Zr/Sm without or with a small concomitant enrichment in Ce/Yb (Fig. 12A). It is striking that most fertile garnet xenocrysts have low Zr/Sm and Ce/Yb ratios, whereas virtually all depleted garnets are enriched in Ce/Yb at low Zr/Sm
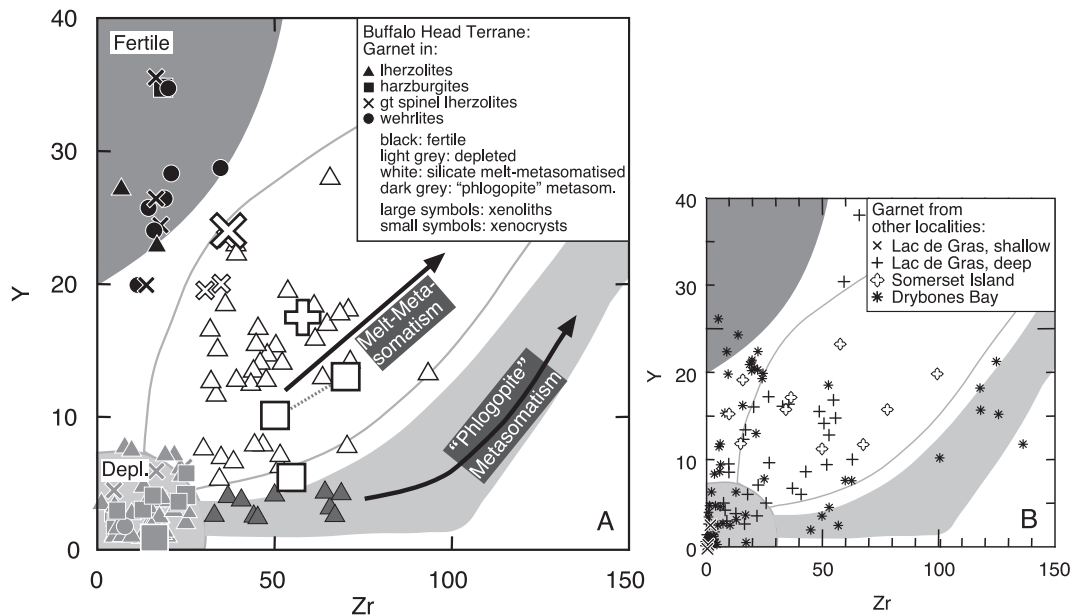

Fig. 10. (A) Zr against Y (ppm) in garnet from xenoliths and xenocrystic garnet. Fields and metasomatic trends of Griffin et al. (1999a). (B) Garnets from the central and marginal Slave craton, and from Somerset Island, are shown for comparison (Lac de Gras, central Slave craton: Pearson et al., 1999; unpublished data; Drybones Bay, Slave craton margin: Carbno and Canil, 2002; Griffin et al., 2004; Somerset Island: Schmidberger and Francis, 1999).
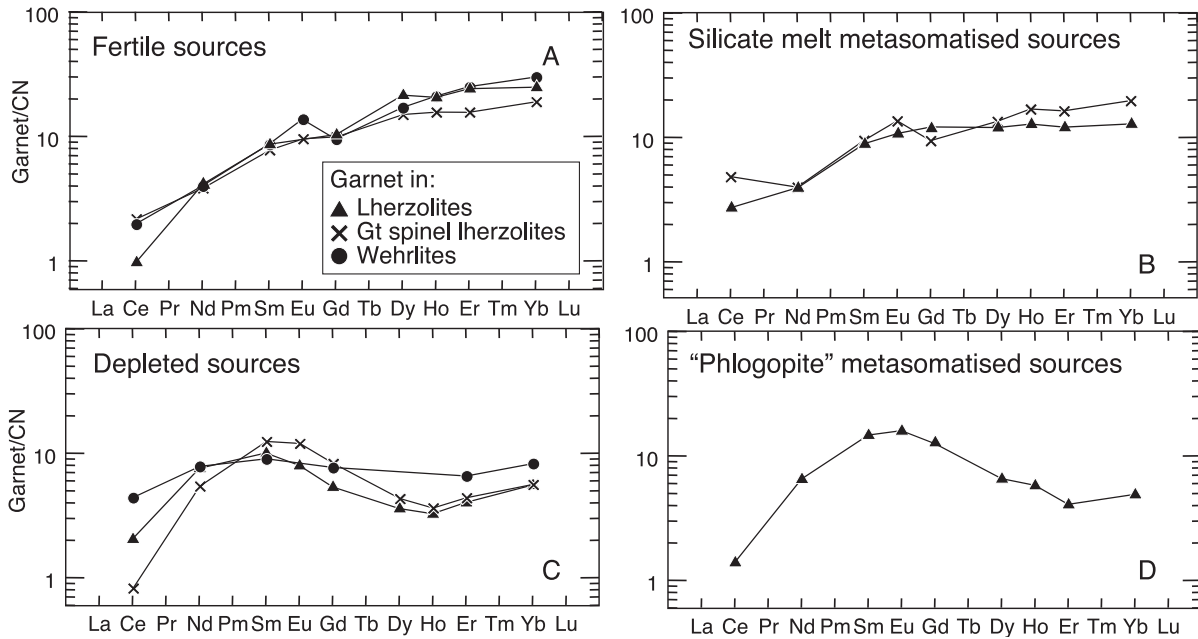
Fig. 11. REE patterns of average garnet xenocryst types (classed according to $CaO-Cr_2O_3$ and $Zr-Y$ relationships) from (A) fertile sources, (B) silicate melt metasomatised sources, (C) depleted sources and (D) "phlogopite" metasomatised sources. Normalised to chondrite of McDonough and Sun (1995).

(Fig. 12B). This is suggested to be a signature of interaction with carbonatite or similar low-volume volatile-rich melt. The sinusoidal REE patterns that are observed in the depleted garnets are ascribed to the steep negative REE pattern of carbonatite, combined with reduced LREE accommodation in garnet due to the increasing size misfit (Griffin et al., 1999b; see also review by Stachel et al., 1998). Samples with positive Eu anomalies do not plot in any particular region of Zr/Sm–Ce/Yb or Zr–Y space. Average "phlogopite" metasomatised lherzolitic garnets are enriched in both Ce/Yb and Zr/Sm. This may indicate that they sequentially interacted with silicate melt and carbonatite (Powell et al., in press), or it may reflect the higher solubility of LREE relative to HFSE in volatile-rich silicate melts such as those that precipitate phlogopite.

The shallow lithosphere (spinel stability field) is represented by garnet spinel peridotites and spinel peridotites, where clinopyroxene is the main host for incompatible elements. A plot of Ti/Eu against La/Yb in clinopyroxene has been used to discriminate between carbonatite and silicate metasomatism (Coltorti et al., 1999) and shows that clinopyroxenes in two of the spinel lherzolites lie between the trends for carbonatite and silicate metasomatism, whereas clinopyroxenes in two other spinel lherzolites have high La/Yb relative to Ti/Eu and may have interacted with carbonatitic melt (Fig. 13). Pure silicate melt metasomatism appears not to have been as important as in the deep lithosphere (garnet stability field), but more data points from the shallow lithosphere are needed to confirm this. A comparison between garnet in Fig. 12A and coexisting clinopyroxene in Fig. 13 is hampered by the absence of either garnet or clinopyroxene in most of the xenolith samples. Furthermore, the scale used by Coltorti et al. (1999) for Phanerozoic and Proterozoic samples may not be appropriate for ancient metasomatised mantle as one clinopyroxene plots far outside the diagram.

Fig. 8A shows that silicate melt metasomatism is the dominant metasomatic style in the deep lithosphere. Depleted and metasomatised rocks, which correspond to volatile-rich silicate melt metasomatised and carbonatite metasomatised sources, occur throughout the lithosphere column but represent the
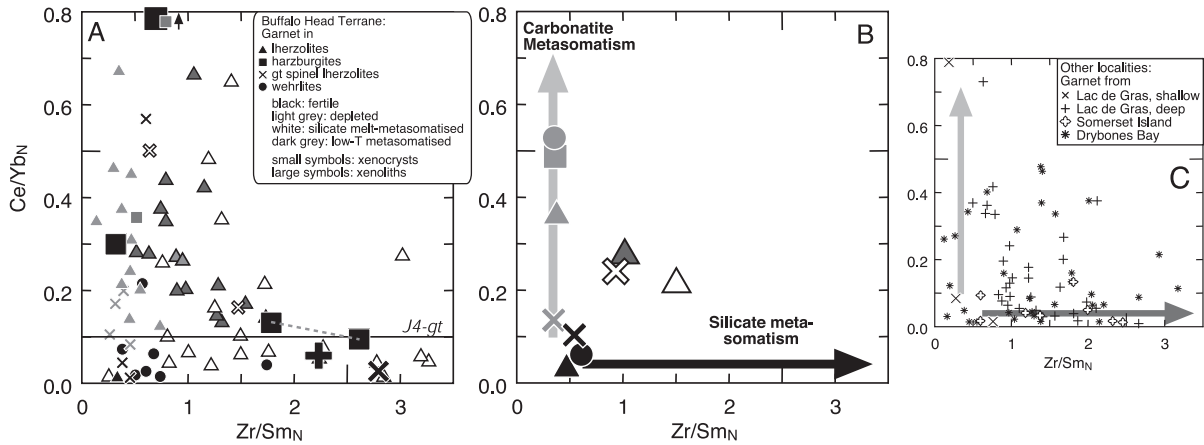
Fig. 12. Zr/Sm_N–Ce/Yb_N relationships (A) in garnet xenocrysts (data of Griffin et al., 2004) and xenoliths; primitive J4-garnet of Jagoutz and Spettel (in Stachel et al., 1998); chondrite of McDonough and Sun (1995), (B) averaged for different garnet classes (see text for details) with trends for silicate and carbonatite metasomatism and (C) in garnets from the central and marginal Slave craton (references as in Fig. 10).

dominant metasomatic style in the shallower lithosphere. This distribution of temperature versus metasomatic style may indicate an evolution of the mantle beneath the BHT similar to that beneath East Africa. During extension in the East African Rift, asthenosphere-derived basaltic melts infiltrated and modified the lower lithosphere; reaction with the surrounding peridotite led to a decrease in the melt volume and evolution of small LILE/LREE/volatile-rich and Nb–Ta-depleted melt fractions that are highly mobile and can penetrate upward in the mantle (Bedini et al., 1997). Signatures of silicate melt metasomatism also occur at shallower depth (e.g., in garnet spinel lherzolites) but, from our limited data set, appear to be volumetrically not as important, perhaps because they are restricted to aureoles along magma conduits (Menzies et al., 1987).

Unradiogenic Nd in the spinel lherzolites indicates ancient enrichment in Nd relative to Sm, which translates into T_{DM} of 2.1 to 2.2 Ga. One spinel lherzolite also has unradiogenic Hf, which would be consistent with enrichment in Hf relative to Lu at least in the Mesoproterozoic. The garnet harzburgites (K11-3 and K11-5) have ε_{Nd} lower than a model depleted mantle indicative of Nd-addition but high ε_{Hf} expected of melt residues. This suggests that Nd, but not Hf, was added at some stage during their evolution and would be typical of carbonatite metasomatism, consistent with the sinusoidal REE patterns of garnets in K11-3 and K11-5. While K11-3 has high Sm/Nd relative to

its Nd isotopic composition, yielding a negative Sm–Nd model age, K11-5 has Sm–Nd isotope systematics that translate into a minimum T_{DM} of 2.1 Ga. By contrast, the Lu/Hf of K11-5 is very low to have produced the amount of radiogenic Hf, indicative of Hf addition at some stage during its evolution. K11-3 gives a Mesoproterozoic Lu–Hf model age. In summary, the isotopic evidence suggests an episode of metasomatism beneath the BHT some time around the Meso- or Paleoproterozoic.

11.4. Young (precursory) heating and metasomatism

Several features in peridotites from Buffalo Hills point to disequilibrium or require high surface energies that are not stable under upper mantle conditions, and therefore appear to be relatively recent. These include compositional disequilibrium, melt patches, secondary overgrowths, exsolution and arrested mineral reactions.

The presence of unequilibrated LREE-enriched garnets (see Fig. 5B) suggests that there was not enough time for diffusive equilibrium to be attained after the enrichment. Ca-undersaturated domains in garnet in sample K11-5 may represent relics of the original depleted composition, whereas high-Ca domains are due to interaction with a metasomatic component.

The major-element composition of the melt patch in sample K14-5b (Fig. 14A) is dissimilar to kim-
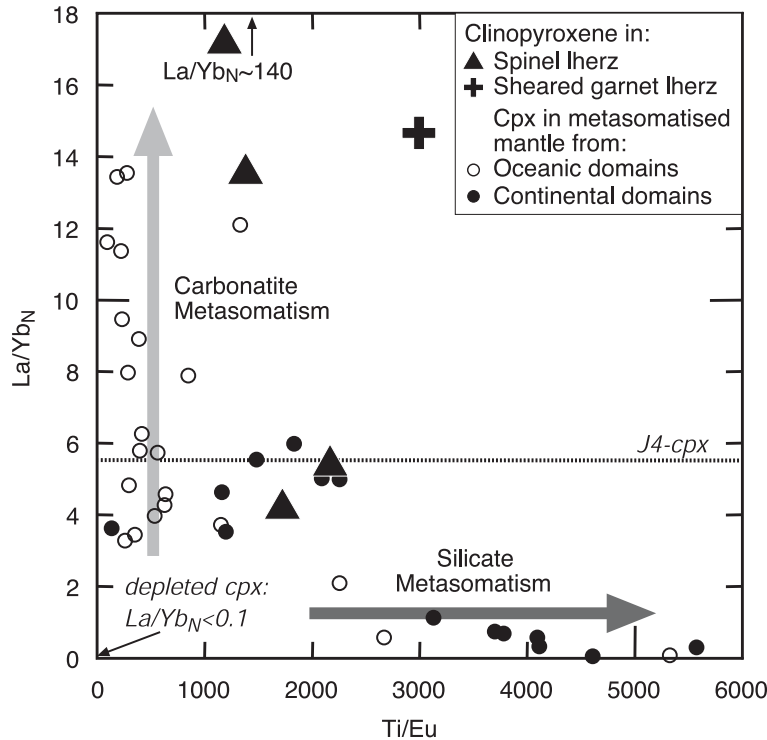
Fig. 13. Ti/Eu against La/Yb$_N$ in cpx from Buffalo Hills. Shown for comparison are clinopyroxenes in carbonatite and silicate melt metasomatised samples from oceanic and continental mantle (from Coltorti et al., 1999). Depleted cpx from Norman (1998), primitive J4 cpx of Jagoutz and Spettel (in Stachel et al., 1998); chondrite of McDonough and Sun (1995).

berlites and intracratonic basalts, and to silicate melt inclusions and melt patches in mantle xenoliths reported in the literature (e.g., Dawson, 1980; Hauri et al., 1993; Schiano and Clocchiatti, 1994; Wiechert et al., 1997; Furman and Graham, 1999). Formation by decompression-induced melting of hydrous phases, such as amphibole (e.g., Chazot et al., 1996), is also precluded by the mismatch in major element content, such as the lack of alkali elements in the melt. By contrast, the high-MgO content, the low contents of other major elements except SiO_2 (FeO below 1 wt.%) and low total oxides obtained by microprobe analysis of the melt patch (see Section 5.8) is similar to volatile-rich ultramafic liquids that occur in spinel lherzolites from Spitsbergen and are interpreted to have exsolved from a primitive volatile-rich magma due to liquid immiscibility (Amundsen, 1987). The ultramafic melt appears to have precipitated spinel and pentlandite, which occur within the melt patches (see Fig. 14A). Precipitation

of many sulfides from a melt may be indicated by their high Si contents (Table 9), ascribed to inclusion of silicate melt during sulfide growth, and by high Re/Os and Os isotopic ratios (Table 13). In addition, most sulfides in xenoliths from the Buffalo Hills kimberlites are pentlandites, which have been interpreted as a metasomatic sulfide (Alard et al., 2000). A secondary origin would be consistent with implausible Re–Os model ages obtained for many sulfides in this study, including one sulfide in the melt patch (sample K14-5b; Table 12).

Most spinels in peridotites from Buffalo Hills have distinct TiO_2-, Cr_2O_3- and Fe^{3+}-rich overgrowths (Fig. 14B), which may indicate interaction with an oxidized silicate melt shortly before entrainment in the kimberlite. Skeletal crystals with compositions similar to the overgrowths are observed in two samples and can be explained by rapid crystallisation from a melt. These phenomena may be related to magmas parental to the megacryst
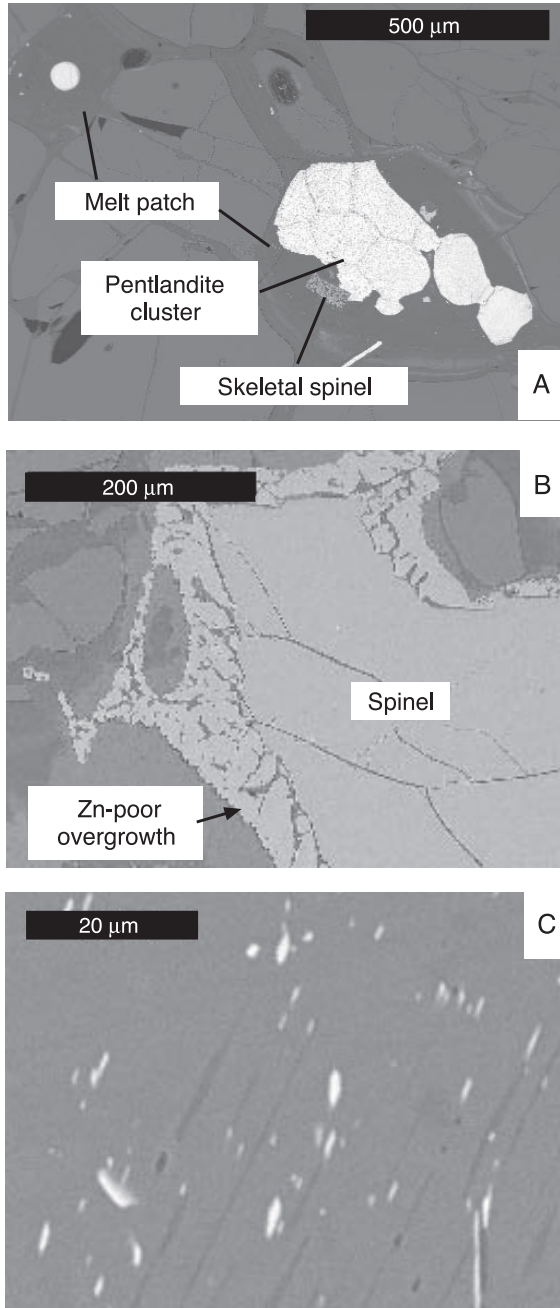
Fig. 14. Backscattered electron images of (A) melt patches containing pentlandite and skeletal spinel, (B) spinel overgrown by Fe^{3+}-, Cr- and Ti-rich, and Zn-poor spinel and (C) cpx with exsolved opx and spinel.

suite which are often temporally related to kimberlite magmatism; their compositions change after fractionation of megacrysts at the base of the lithosphere and assimilation of peridotitic wall-rock during ascent, becoming more Fe- and Ti- rich (e.g., Griffin et al., 2000). Overprinting by similar Ti-rich oxidizing magmas that acquired high Cr contents through interaction with the lithospheric mantle may explain secondary overgrowths on preexisting spinels.

The similarity of the composition of secondary overgrowths to skeletal spinel in the melt patch in sample K14-5b suggests that, like the precipitation of some pentlandites, these are manifestations of the same event. The infiltration of melts was accompanied by heating of the lithosphere, consistent with the lower Zn contents observed in spinel overgrowths and skeletal spinel, as Zn abundance in spinel decreases with increasing temperature (Griffin et al., 1994).

The solubility of the enstatite component in clinopyroxene and of the diopside component in orthopyroxene is temperature dependent (Brey and Köhler, 1990). Therefore, the ubiquitous exsolution of complementary pyroxene from clinopyroxenes and orthopyroxenes in spinel lherzolites (Fig. 14C) records cooling, subsequent to the heating and melt intrusion described above. Garnet and spinel in a garnet spinel lherzolite xenolith share amoeboid and vermicular grain boundaries (see Fig. 2B) that represent high energy states that cannot survive for extended periods of time in the upper mantle (e.g., Field and Haggerty, 1994). This indicates that there was not enough time for these grains to texturally re-equilibrate before entrainment in the kimberlite.

Many of the samples that show evidence for heating and young metasomatism are stored in the shallow mantle at relatively low temperatures, which could have prevented equilibration for substantial amounts of time. Therefore, disequilibrium features do not constrain the timing of the disturbance to immediately preceding entrainment in the kimberlite. They do, however, establish a sequence of events where these phenomena postdate the older modification of the mantle that is manifest in equilibrated assemblages with homogeneous compositions.

11.5. Pyroxenite genesis

Several pyroxenites show evidence for cooling and re-equilibration from high temperatures. One sample with corona and necklace structures is interpreted to have preserved at least three stages of re-equilibration. The garnet corona and orthopyroxene- and clinopyroxene-rich domains may have originated during an initial stage of exsolution from high-temperature Al-rich and Ca-poor clinopyroxene during cooling, as suggested for garnet pyroxenites from eastern Australia (Griffin et al., 1984; O'Reilly et al., 1988; Pearson et al., 1991). In a second phase, both the orthopyroxene and clinopyroxene domains exsolved garnet, now arranged as necklaces. In a third phase, large grains of orthopyroxene and clinopyroxene exsolved spinel and pyroxenes, and garnet exsolved rutile. The garnet corona protected the assemblages in each of the domains and slowed diffusive exchange and equilibration (e.g., Pearson et al., 1991). For example, garnet within the orthopyroxene domain has higher FeO and lower MgO than garnet in other domains. Clinopyroxene on either side of the garnet corona has distinct Al_2O_3, CaO and Na_2O contents. Garnet necklaces around orthopyroxene, without marked corona structures, are observed in other pyroxenites and suggest a more advanced state of re-equilibration subsequent to cooling-related exsolution.

Garnet and clinopyroxene from Buffalo Hills pyroxenites and those from eastern Australia have compositions that partially overlap and show similar trends (Fig. 15). Garnet pyroxenites from eastern Australia are suggested to have formed during underplating of mafic magmas into the lower crust and upper mantle (Wass and Hollis, 1983). Pyroxenites from Buffalo Hills may have a similar origin. Cooling to the ambient geotherm led to progressive exsolution and reaction processes that were arrested at low temperatures.

11.6. Comparison with Slave craton mantle sections

Mantle sections from the Slave craton include the north-central Jericho kimberlites (Kopylova et al., 1999; Griffin et al., 1999c), central Lac de Gras kimberlites (Pearson et al., 1999; Griffin et al., 1999c; 2004), the Torrie kimberlite which lies between the two (Griffin et al., 1999c; MacKenzie and Canil, 1999; Orr and Luth, 2000) and the Drybones Bay kimberlite at the craton margin (Carbno and Canil, 2002; Griffin et al., 2004). The mantle beneath Jericho and Torrie may have been reworked in connection with formation of the Kilohigok basin (Griffin et al., 1999c) or the 1.27 Ga Mackenzie plume event (Irvine et al., 1999). The mantle beneath Drybones Bay may have been heated and strongly metasomatised (Carbno and Canil, 2002) and may have been reworked or entirely replaced during the Proterozoic in the course of subduction events, or of movement along the Great Slave Lake shear zone (Griffin et al., 1999c).

With regard to major-element composition, reconstructed peridotites from Buffalo Hills have a range in FeO, MgO and SiO_2 similar to those in the deeper layer of the Archaean central Slave craton (Fig. 9). It is conceivable that samples that have not been silicate melt-metasomatised have preserved major-element relationships that were established during the melting related to lithosphere formation. If so, this would suggest that the mantle beneath the BHT and the central Slave craton formed under similar conditions. The lower lithosphere of the central Slave craton is suggested to have formed by subcretion of a plume that originated in the lower mantle (Griffin et al., 1999c). Inclusions in diamond from the Buffalo Hills kimberlites encompass minerals from the transition zone and the lower mantle as well as mixed parageneses, and the host diamonds are suggested to have grown in a plume (Davies et al., 2003), strengthening the plume connection.

For peridotites from both BHT and central Slave craton, there is a negative correlation of SiO_2 and FeO that is displaced toward higher SiO_2 relative to peridotites from the Kaapvaal and Siberian cratons, which are characterised by high orthopyroxene/olivine ratios. This suggests that, whatever the mechanism by which ancient lithosphere is enriched in orthopyroxene relative to olivine (see review by Walter, 1998), it differed for the mantle beneath the BHT and central Slave craton on the one hand and the Kaapvaal and Siberian cratons on the other.

Garnets from the Slave craton margin setting (Drybones Bay) have a range of Zr–Y relationships similar to garnets from the BHT (Fig. 10B), although
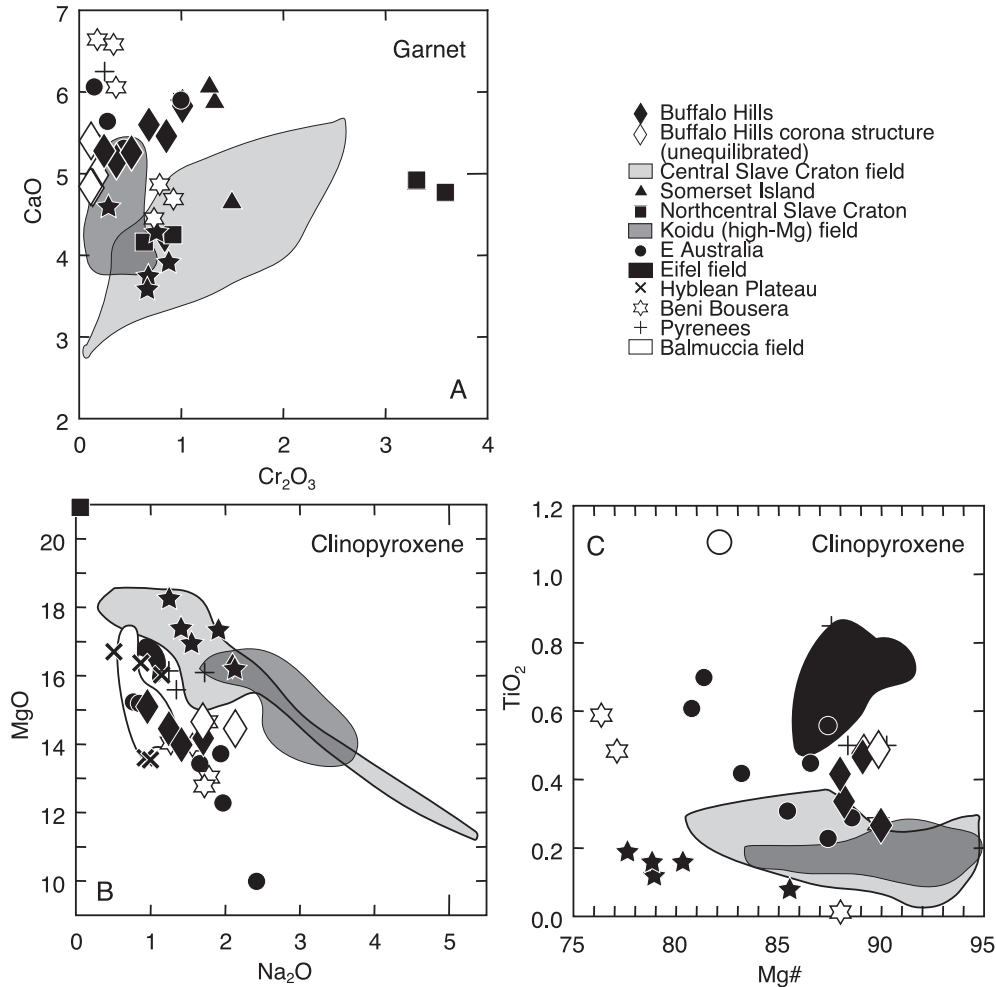
Fig. 15. (A) Cr_2O_3 against CaO in garnet, (B) Na_2O against MgO in cpx and (C) Mg# against TiO_2 in cpx in pyroxenites from Buffalo Hills. Shown for comparison are pyroxenite xenoliths and pyroxenites in peridotite massifs (Beni Bousera, Morocco: Kornprobst, 1969; Pyrenées: Bodinier et al., 1987; Balmuccia: Rivalenti et al., 1995; Eastern Australia: O'Reilly and Griffin, 1995; Hyblean Plateau, Sicily: Nimis and Vannucci, 1995; Eifel volcanic fields, Germany: Witt-Eickschen et al., 1998; other references as in Fig. 10).

carbonatite metasomatism appears to have been much more important for the mantle beneath the BHT (Fig. 12C). This similarity could stem from the fact that the mantle across the BHT, because it is a narrow continental block, has been affected by processes at its margins, such as rifting, similar to the mantle beneath Drybones Bay. In contrast, trace-element relationships differ for the central Slave craton in that garnets from fertile and "phlogopite" metasomatised sources are absent, and this may reflect its position in the craton interior, away from processes occurring at the craton margins.

12. Summary and conclusions

Several features of peridotites from the Buffalo Hills kimberlites hint at the presence of Archaean mantle beneath the BHT. Sinusoidal trace element patterns resemble those of inclusions in diamond occurring in Archaean cratonic areas of the world, and diamonds have been recovered from host kimberlites. The occurrence of relict Ca-undersaturated Cr_2O_3-rich garnet in one of the garnet harzburgites may be an Archaean inheritance because true Ca-undersaturated garnet is virtually exclusive to Archae-

an SCLM (Griffin et al., 1998). However, there is no unequivocal isotopic evidence for Archaean mantle.

The SCLM beneath the BHT experienced at least two episodes of modification. The oldest recognised metasomatic event is suggested to be responsible for enriched trace-element abundances in compositionally equilibrated xenoliths. Three metasomatic styles are recognised: silicate melt metasomatism, carbonatite metasomatism and an intermediate style possibly involving volatile-rich silicate melt. Silicate melt metasomatism prevailed in the deep lithosphere and led to enrichment of HFSE with minor enrichment in LREE. Carbonatite metasomatism and volatile-rich melt metasomatism led to enrichment of LREE without, or with only a small, concomitant enrichment in HFSE, respectively. These metasomatic styles are more common in the shallower lithosphere. This distribution of metasomatic styles in the lithosphere column is interpreted in terms of a model, whereby rift-related asthenosphere-derived silicate melts extensively interact with the mantle close to the lithosphere–asthenosphere boundary, which leads to formation of more mobile residual volatile-rich melts that are able to penetrate shallower lithosphere levels (Bedini et al., 1997). Rifting-related metasomatism of the SCLM beneath the BHT may have occurred between 2.4–2.1 Ga ago, when the BHT and adjacent Rae Province were separated by oceanic crust (Bostock and van Breemen, 1994; McNicoll et al., 2000). Clinopyroxenes with 2.10–2.25 Nd model ages in two spinel lherzolites may be related to this event.

Mesoproterozoic Re–Os T_{CHUR} model ages were obtained for sulfides in two spinel peridotites. The 1.74 Ga model age obtained for sulfide in sample K14-5b is considered fortuitous because this sulfide has highly radiogenic Os and very high Re/Os ratio requiring large corrections for the overlap of ^{187}Re on ^{187}Os. In addition, a second analysis of sulfides in this sample revealed that the Re–Os isotope systematics and resultant model ages are variable. By contrast, sulfide in K14-5d is the only sample of all samples measured that has a low Re/Os and unradiogenic Os isotopic composition. The minimum age (Re-depletion age, T_{RD}; Walker et al., 1989) is 1.46 Ga; the model age of 1.84 Ga is considered to reflect the true age of this sulfide. This age coincides with the inferred emplacement age of the mafic sheets of the

Winagami Reflection Sequence in the crust (WRS; Ross and Eaton, 1997) and suggests that the sulfide precipitated from melts related to this igneous event. Emplacement of mafic dykes and sills may be related to impingement of a plume at the base of the lithosphere (e.g., 1.27 Ga Mackenzie plume and dike swarm; LeCheminant and Heaman, 1989). The presence of magmatic mantle sulfide having a similar age to the igneous sheets may indicate that the plume source was located beneath the BHT, and that the lithospheric mantle interacted with the plume-derived melts at about 1.9 to 1.8 Ga. Garnet in the pyroxenite K14-5f gives an Nd model age of 1.8 Ga. This may indicate that pyroxenites also formed from the asthenosphere-derived melts parental to the mafic sheets of the WRS but were stored at temperatures too low to allow textural re-equilibration.

A younger metasomatic event occurred some time before kimberlite magmatism at 88–86 Ma. Heating and interaction with oxidizing silicate melts are indicated by heterogeneous mineral compositions, overgrowths on spinel that are Ti- and Fe^{3+}-rich but Zn-poor and the occurrence of melt patches. Fine-scale exsolutions of orthopyroxene and clinopyroxene in the complementary pyroxene are observed in many samples and testify to subsequent cooling. Some of these magmas may have pooled at shallower depth where they exsolved ultramafic volatile-rich liquids similar to melt patches found in one spinel lherzolite. Megacryst magmas are inferred to be temporally, although not necessarily genetically, related to kimberlite magmatism (e.g., Griffin et al., 2000). Migration of such melts may have heated and interacted with the mantle prior to eruption of the kimberlites. The isotope data set shows that some samples have unsupported radiogenic Hf or Nd or high parent/daughter ratios relative to their isotopic composition and this may also relate to relatively recent decoupling of parent and daughter elements during metasomatism.

Our data show that samples from the SCLM beneath the BHT are witnesses to multiple metasomatic episodes, and it is plausible that these processes are linked to events expressed at crustal levels. The emplacement of plume-derived diamonds (Davies et al., 2003) may have occurred during rifting at 2.4–2.3 Ga, assuming this event was caused by a plume. Alternatively, formation of these diamonds may be

related to intrusion of the mafic sills of the Winagami Reflection Sequence at ~ 1.8 Ga, which may be plume-related similar to the prominent Mackenzie dike swarm in the Slave craton. The variety of events documented within the BHT and along its margins may well have obliterated any unambiguous Archaean signature that was originally present.

Acknowledgements

References

Alard, O., Griffin, W.L., Lorand, J.P., Jackson, S.E., O'Reilly, S.Y., 2000. Non-chondritic distribution of the highly siderophile elements in mantle sulfides. Nature 407, 891–894.

Amundsen, H.E.F., 1987. Evidence for liquid immiscibility in the upper mantle. Nature 327, 692–695.

Bedini, R.M., Bodinier, J.-L., Dautria, J.-M., Morten, L., 1997. Evolution of LILE-enriched small melt fractions in the lithospheric mantle: a case study from the East African Rift. Earth Planet. Sci. Lett. 153, 67–83.

Blichert-Toft, J., 2001. On the Lu-Hf Isotope Geochemistry of Silicate Rocks. J. Geost. Geoanal. 25, 41–56.

Blichert-Toft, J., Albarède, F., 1997. The Lu–Hf isotope geochemistry of chondrites and the evolution of the mantle–crust system. Earth Planet. Sci. Lett. 148, 243–258.

Blichert-Toft, J., Chauvel, C., Albarède, F., 1997. Separation of Hf and Lu for high precision isotope analysis of rock samples by magnetic sector-multiple collector ICPMS. Contrib. Mineral. Petrol. 127, 248–260.

Bodinier, J.J., Guiraud, M., Fabries, J., Dostal, J., Dupuy, C., 1987. Petrogenesis of layered pyroxenites from the Lherz, Freychinède and Prades ultramafic bodies (Ariège, French Pyrénées). Geochim. Cosmochim. Acta 51, 279–290.

Bostock, H., van Breemen, O., 1994. Ages of detrital and metamor-phic zircons and monazites from a pre-Taltson magmatic zone basin at the western margin of Rae Province. Can. J. Earth Sci. 31, 1353–1364.

Brey, G.P., Köhler, T., 1990. Geothermobarometry in four-phase lherzolites: II. New thermobarometers, and practical assessment of existing thermobarometers. J. Petrol. 31, 1353–1378.

Carbno, G.B., Canil, D., 2002. Mantle structure beneath the SW Slave craton, Canada: constraints from garnet geochemistry in the Drybones Bay kimberlite. J. Petrol. 43, 129–142.

Carlson, S.M., Hillier, W.D., Hood, C.T., Pryde, R.P., Skelton, D.N., 1999. The Buffalo Hills kimberlites: a newly-discovered diamondiferous kimberlite province in north-central Alberta, Canada. In: Gurney, J.J., Gurney, J.L., Pascoe, M.D., Richardson, S.H. (Eds.), Proc. 7th Intl. Kimb. Conf. Red Roof Design cc, Cape Town, pp. 109–116.

Chazot, G., Menzies, M.A., Harte, B., 1996. Determination of partition coefficients between apatite, clinopyroxene, amphibole, and melt in natural lherzolites from Yemen: implications for wet melting in the lithospheric mantle. Geochim. Cosmochim. Acta 60, 423–437.

Coltorti, M., Bonadiman, C., Hinton, R.W., Siena, F., Upton, B.G.J., 1999. Carbonatite metasomatism of the oceanic upper mantle: evidence from clinopyroxenes and glasses in ultramafic xenoliths of Grande Comore, Indian Ocean. J. Petrol. 40 (1), 133–165.

Coltorti, M., Beccaluva, L., Bonadiman, C., Salvini, L., Siena, F., 2000. Glasses in mantle xenoliths as geochemical indicators of metasomatic agents. Earth Planet. Sci. Lett. 183, 303–320.

Davies, R.M., Griffin, W.L., O'Reilly, S.Y., McCandless, T.E., 2003. Inclusions in diamonds from the K10 and K14 kimberlites, Buffalo Hills, Alberta, Canada: diamond growth in a plume? Ext. Abstr., 8th Intl. Kimb. Conf., Victoria BC.

Dawson, J., 1980. Kimberlites and Their Xenoliths. Springer, Berlin 252 pp.

DePaolo, D.J., 1981. Neodymium isotopes in the Colorado Front Range and crust–mantle evolution in the Proterozoic. Nature 291, 193–196.

Droop, G., 1987. A general equation for estimating Fe^{3+} concentrations in ferromagnesian silicates and oxides from microprobe analyses, using stoichiometric criteria. Geol. Mag. 51, 431–435.

Ellis, D., Green, D., 1979. An experimental study of the effect of Ca upon garnet–clinopyroxene Fe–Mg exchange equilibria. Contrib. Mineral. Petrol. 71, 13–22.

Field, S., Haggerty, S., 1994. Symplectites in upper mantle peridotites: development and implications for the growth of subsolidus garnet, pyroxene and spinel. Contrib. Mineral. Petrol. 118, 138–156.

Furman, T., Graham, D., 1999. Erosion of lithospheric mantle beneath the East African Rift system: geochemical evidence from the Kivu volcanic province. Lithos 48, 237–262.

Gaul, O.F., Griffin, W.L., O'Reilly, S.Y., Pearson, N.J., 2000. Mapping olivine composition in the lithospheric mantle. Earth Planet. Sci. Lett. 182, 223–235.

Griffin, W.L., Wass, S.Y., Hollis, J.D., 1984. Ultramafic xenoliths from Bullenmerri and Gnotuk Maars, Victoria, Australia: petrology of a sub-continental crust–mantle transition. J. Petrol. 25, 53–87.

Griffin, W.L., Smith, D., Boyd, F.R., 1987. Trace-element zoning in garnets from sheared mantle xenoliths. Geochim. Cosmochim. Acta 53, 561–567.

Griffin, W.L., Ryan, C.G., Gurney, J.J., Sobolev, N.V., Win, T.T., 1994. Chromite macrocrysts in kimberlites and lamproites: geochemistry and origin. In: Meyer, H., Leonardo, O. (Eds.), Kimberlites, Related Rocks and Mantle Xenoliths. CPRM Spec. Publ., Brasilia, pp. 366–377. Jan/94.

Griffin, W., O'Reilly, S., Ryan, C., Gaul, O., Ionov, D., 1998. Secular variation in the composition of subcontinental lithospheric mantle. In: Braun, J., Dooley, J., Goleby, B., van der Hilst, R., Klootwijk, C. (Eds.), Structure and Evolution of the Australian Continent. Geodynamics Series. Amer. Geophys. Union, Washington, DC, pp. 1–26.

Griffin, W.L., Shee, S.R., Ryan, C.G., Win, T.T., Wyatt, B.A., 1999a. Harzburgite to lherzolite and back again: metasomatic processes in ultramafic xenoliths from the Wesselton kimberlite, Kimberley, South Africa. Contrib. Mineral. Petrol. 134 (2–3), 232–250.

Griffin, W.L., Fisher, N.I., Friedman, J.H., Ryan, C.G., O'Reilly, S.Y., 1999b. Cr-pyrope garnets in the lithospheric mantle. I: compositional systematics and relations to tectonic setting. J. Petrol. 40, 679–705.

Griffin, W.L., Doyle, B.J., Ryan, C.G., Pearson, N.J., O'Reilly, S.Y., Davies, R.M., Kivi, K., Van Achterbergh, E., Natapov, L.M., 1999c. Layered mantle lithosphere in the Lac de Gras Area, Slave craton: composition, structure and origin. J. Petrol. 40, 705–727.

Griffin, W.L., Pearson, N.J., Belousova, E., Jackson, S.E., van Achterbergh, E., O'Reilly, S.Y., Shee, S.R., 2000. The Hf isotope composition of cratonic mantle: LAM–MC–ICPMS analysis of zircon megacrysts in kimberlites. Geochim. Cosmochim. Acta 64, 133–147.

Griffin, W.L., Fisher, N.I., Friedman, J.H., O'Reilly, S.Y., Ryan, C.G., 2002. Cr-pyrope garnets in the lithospheric mantle: II. Compositional populations and their distribution in time and space. Geochem. Geophys. Geosyst. 3, 1073.

Griffin, W.L., O'Reilly, S.Y., Abe, N., Aulbach, S., Davies, R.M., Pearson, N.J., Doyle, B.J., Kivi, K., 2003. The origin and evolution of Archean lithospheric mantle. Precambrian Res. 127, 19–41.

Griffin, W.L., O'Reilly, S.Y., Doyle, B.J., Kivi, K., 2004. Lithospheric Mapping Beneath the North American Plate. Lithos 77, 873–922 (this volume).

Gurney, J., 1984. A correlation between garnets and diamonds in kimberlites. Publ. Geol. Dept. & Univ. Extension, vol. 8. Univ. West Aust, Perth, pp. 143–166.

Harley, S., 1984. An experimental study of the partitioning of iron and magnesium between garnet and orthopyroxene. Contrib. Mineral. Petrol. 86, 359–373.

Hauri, E.H., Shimizu, N., Dieu, J.J., Hart, S.R., 1993. Evidence for hotspot-related carbonatite metasomatism in the oceanic upper mantle. Nature 365, 221–227.

Hauri, E.H., Wagner, T.P., Grove, T.L., 1994. Experimental and natural partitioning of Th, U, Pb and other trace elements between garnet, clinopyroxene and basaltic melts. Chem. Geol. 117, 149–166.

Hoffman, P.F., 1989. Precambrian geology and tectonic history of North America. In: Bally, A., Palmer, A. (Eds.), The Geology of North America—An Overview. Geol. Soc. Amer., 447–512.

Hood, C.T., McCandless, T.E., 2003. Systematic variations in xenocryst mineral composition at the province scale, Buffalo Hills kimberlites, Alberta, Canada. Ext. Abstr., 8th Intl. Kimb. Conf., Victoria BC.

Ionov, D., 1998. Trace element composition of mantle-derived carbonate and coexisting phases in peridotite xenoliths from alkali basalts. J. Petrol. 39, 1931–1941.

Irvine, G.J., Kopylova, M.G., Carlson, R.W., Pearson, D.G., Shirey, S.B., Kjarsgaard, B.A., 1999. Age of the lithospheric mantle beneath and around the Slave craton: a Re–Os isotope study of peridotite xenoliths from the Jericho and Somerset Island kimberlites. Abstr. 9th Goldschmidt Conf. LPI, Boston, MA, pp. 134–135.

Jerde, E.A., Taylor, L.A., Crozaz, G., Sobolev, N.V., Sobolev, V.N., 1993. Diamondiferous eclogites from Yakutia, Siberia—evidence for a diversity of protoliths. Contrib. Mineral. Petrol. 114, 189–202.

Kempton, P.D., Hawkesworth, C.J., Lopez-Escobar, L., Pearson, D.G., Ware, A.J., 1999. Spinel ± garnet lherzolite xenoliths from Pali Aike. Part 2: trace element and isotopic evidence bearing on the evolution of lithospheric mantle beneath southern Patagonia. In: Gurney, J.J., Gurney, J.L., Pascoe, M.D., Richardson, S.H. (Eds.), 7th Intl. Kimberlite Conf. Red Roof Design cc, Cape Town, pp. 415–428.

Kennedy, C., Kennedy, G., 1976. The equilibrium boundary between graphite and diamond. J. Geophys. Res. 81, 2467–2470.

Klemme, S., van der Laan, S.R., Foley, S.F., Guenther, D., 1995. Experimentally determined trace and minor element partitioning between clinopyroxene and carbonatite melt under upper mantle conditions. Earth Planet. Sci. Lett. 133, 439–448.

Kopylova, M.G., Russell, J.K., Cookenboo, H., 1999. Petrology of peridotite and pyroxenite xenoliths from the Jericho kimberlite: implications for the thermal state of the mantle beneath the Slave craton, Northern Canada. J. Petrol. 40 (1), 79–104.

Kopylova, M.G., Russell, J.K., Stanley, C., Cookenboo, H., 2000. Garnet from Cr and Ca-saturated mantle: implications for diamond exploration. J. Geochem. Explor. 68, 183–199.

Kornprobst, J., 1969. Le massif ultrabasique des Beni Bouchera (Rif Interne, Maroc): Etude des peridotites de haute temperature et de haute pression, et des pyroxénolites, a grenat ou sans grenat. Contrib. Mineral. Petrol. 23, 283–322.

Krogh, E., 1988. The garnet–clinopyroxene iron–magnesium geothermometer—a reinterpretation of existing experimental data. Contrib. Mineral. Petrol. 99, 44–48.

LeCheminant, A.N., Heaman, L.M., 1989. Mackenzie igneous events, Canada: middle Proterozoic hotspot magmatism associated with ocean opening. Earth Planet. Sci. Lett. 96, 38–48.

Lee, C.-T., Rudnick, R.L., 1999. Compositionally stratified cratonic lithosphere: petrology and geochemistry of peridotite xenoliths from the Labait tuff cone, Tanzania. In: Gurney, J.J., Gurney, J.L., Pascoe, M.D., Richardson, S.H. (Eds.), Proc. 7th Int. Kimb. Conf. Red Roof Design cc, Cape Town, pp. 503–521.

MacKenzie, J.M., Canil, D., 1999. Composition and thermal evolution of cratonic mantle beneath the central Archean

Slave Province, NWT, Canada. Contrib. Mineral. Petrol. 134, 313–324.

McDonough, W.F., Sun, S.-S., 1995. The composition of the Earth. Chem. Geol. 120, 223–253.

McNicoll, V.J., Thériault, R.J., McDonough, M.R., 2000. Taltson basement gneissic rocks: U–Pb and Nd isotopic constraints on the basement to the Paleoproterozoic Taltson magmatic zone, northeastern Alberta. Can. J. Earth Sci. 37, 1575–1596.

Menzies, M.A., Rogers, N., Tindle, A., Hawkesworth, C.J., 1987. Metasomatic and enrichment processes in lithospheric peridotites, an effect of asthenosphere–lithosphere interaction. In: Menzies, M.A., Hawkesworth, C.J. (Eds.), Mantle Metasomatism. Academic Press, London, pp. 313–361.

Nickel, K.G., Green, D.H., 1985. Empirical geothermobarometry for garnet peridotites and implications for the nature of the lithosphere, kimberlites and diamonds. Earth Planet. Sci. Lett. 73 (1), 158–170.

Nimis, P., Vannucci, R., 1995. An ion microprobe study of clinopyroxenes in websteritic and megacrystic xenoliths from Hyblean Plateau (Se Sicily, Italy)—constraints On HFSE/REE/Sr fractionation at mantle depth. Chem. Geol. 124 (3–4), 185–197.

Norman, M.D., 1998. Melting and metasomatism in the continental lithosphere: laser ablation ICPMS analysis of minerals in spinel lherzolites from Eastern Australia. Contrib. Mineral. Petrol. 130, 240–255.

Norman, M.D., Pearson, N.J., Sharma, A.L., Griffin, W.L., 1996. Quantitative analysis of trace elements in geological materials by laser ablation ICPMS: instrumental operating conditions and calibration values of NIST glasses. Geostand. Newsl. 20 (2), 247–261.

O'Neill, H., Wood, B., 1979. An experimental study of the iron–magnesium partitioning between garnet and olivine and its calibration as a geothermometer. Contrib. Mineral. Petrol. 70, 59–70.

O'Reilly, S.Y., Griffin, W.L., 1995. Trace-element partitioning between garnet and clinopyroxene in mantle-derived pyroxenites and eclogites—P–T–X controls. Chem. Geol. 121 (1–4), 105–130.

O'Reilly, S.Y., Griffin, W.L., Stabel, A., 1988. Evolution of Phanerozoic Eastern Australian lithosphere: isotope evidence for magmatic and tectonic underplating. J. Petrol., Spec, 89–108.

Orr, P., Luth, R.W., 2000. Petrology and oxygen-isotope geochemistry of the Yamba Lake kimberlite rocks, NWT. Can. J. Earth Sci. 37, 1053–1071.

Patchett, P.J., Tatsumoto, M., 1980. Hafnium isotope variations in oceanic basalts. Geophys. Res. Lett. 7, 1077–1080.

Pearson, N.J., O'Reilly, S.Y., Griffin, W.L., 1991. The granulite to eclogite transition beneath the eastern margin of the Australian craton. Eur. J. Mineral. 3 (2), 293–322.

Pearson, N.J., Griffin, W.L., Doyle, B.J., O'Reilly, S.Y., van Achterbergh, E., Kivi, K., 1999. Xenoliths from kimberlite pipes of the Lac de Gras area, Slave craton, Canada. In: Gurney, J.J., Gurney, M.D., Pascoe, M.D., Richardson, S.H. (Eds.), 7th Intl. Kimberlite Conf. Red Roof Design cc, Cape Town, pp. 644–658.

Pearson, N.J., Alard, O., Griffin, W.L., Jackson, S.E., O'Reilly, S.Y., 2002. In situ measurement of Re–Os isotopes in mantle sulfides by laser ablation multicollector-

inductively coupled plasma mass spectrometry: analytical methods and preliminary results. Geochim. Cosmochim. Acta 66, 1037–1050.

Pollack, H.N., Chapman, D.S., 1977. On the regional variation of heat flow, geotherms, and lithospheric thickness. Tectonophys 38, 279–296.

Pouchou, J.L., Pichoir, F., 1984. A new model for quantitative X-ray microanalysis of homogeneous samples. Rech. Aérosp. 5, 13–38.

Powell, W., Zhang, M., O'Reilly, S.Y., Tiepolo, M., 2004. Mantle amphibole trace-element and isotopic signatures trace multiple metasomatic episodes in lithospheric mantle, western Victoria, Australia. Lithos (in press).

Rivalenti, G., Mazzucchelli, M., Vannucci, R., Hofmann, A.W., Ottolini, L., Bottazzi, P., Obermiller, W., 1995. The relationship between websterite and peridotite in the Balmuccia peridotite massif (NW Italy) as revealed by trace element variations in clinopyroxene. Contrib. Mineral. Petrol. 121, 275–288.

Ross, G.M., 2000. Introduction to special issue of Canadian Journal of Earth Sciences: the Alberta basement transect of lithoprobe. Can. J. Earth Sci. 37, 1447–1452.

Ross, G.M., 2002. Evolution of Precambrian continental lithosphere in western Canada: results from lithoprobe studies in Alberta and beyond. Can. J. Earth Sci. 39, 413–437.

Ross, G.M., Eaton, D.W., 1997. Winagami reflection sequence: seismic evidence for post-collisional magmatism in the Proterozoic of western Canada. Geology 25, 199–202.

Ross, G.M., Eaton, D.W., 2002. Proterozoic tectonic accretion and growth of western Laurentia: results from lithoprobe studies in northern Alberta. Can. J. Earth Sci. 39, 313–329.

Ross, G.M., Parrish, R.R., Villeneuve, M.E., Bowring, S.A., 1991. Geophysics and geochronology of the crystalline basement of the Alberta basin, western Canada. Can. J. Earth Sci. 28, 512–522.

Ross, G.M., Eaton, D.W., Boerner, D.W., Miles, W., 2000. Tectonic entrapment and its role in the evolution of the continental lithosphere: an example from the Precambrian of western Canada. Tectonics 19, 116–134.

Rudnick, R.L., McDonough, W.F., Chappell, B.W., 1993. Carbonatite metasomatism in the northern Tanzanian mantle: petrographic and geochemical characteristics. Earth Planet. Sci. Lett. 114, 463–475.

Ryan, C.G., Griffin, W.L., Pearson, N.J., 1996. Garnet geotherms—pressure–temperature data from Cr-pyrope garnet xenocrysts in volcanic rocks. J. Geophys. Res. 101 (B3), 5611–5625.

Schiano, P., Clocchiatti, R., 1994. Worldwide occurrence of silica-rich melts in sub-continental and sub-oceanic mantle minerals. Nature 368, 621–624.

Schmidberger, S., Francis, D., 1999. Nature of the mantle roots beneath the North American craton: mantle xenolith evidence from Somerset Island kimberlites. Lithos 48, 195–216.

Smith, D., 1999. Temperatures and pressures of mineral equilibration in peridotite xenoliths: review, discussion, and implications. In: Fei, Y., Bertka, C.M., Mysen, B.O. (Eds.), Mantle Petrology: Field Observations and High Pressure Experimentation: A Tribute to Francis R. (Joe) Boyd. Spec. Publ. - Geochem. Soc., vol. 6, pp. 171–188.

Smith, D., Boyd, F.R., 1987. Compositional heterogeneities in a high-temperature lherzolite nodule and implications for mantle processes. In: Nixon, P.H. (Ed.), Mantle Xenoliths. Wiley, New York, pp. 551–561.

Sobolev, N., Lavrent'yev, Y., Pokhilenko, N., Usova, L., 1973. Chrome-rich garnets from the kimberlites of Yakutia and their paragenesis. Contrib. Mineral. Petrol. 40, 39–52.

Stachel, T., Viljoen, K.S., Brey, G., Harris, J.W., 1998. Metasomatic processes in lherzolitic and harzburgitic domains of diamondiferous lithospheric mantle: REE in garnets from xenoliths and inclusions in diamonds. Earth Planet. Sci. Lett. 159 (1–2), 1–12.

Thériault, R.J., Ross, G.M., 1991. Nd isotopic evidence for crustal recycling in the ca. 2.0 Ga subsurface of western Canada. Can. J. Earth Sci. 28, 1149–1157.

van Achterberg, E., Ryan, C.G., Griffin, W.L., 1999. Glitter: on line intensity reduction for the laser ablation inductively coupled plasma spectrometry. Abstr. 9th Goldschmidt Conf. LPI, Boston, MA, pp. 905.

Walker, R.J., Carlson, R.W., Shirey, S.B., Boyd, F.R., 1989. Os, Sr, Nd, and Pb isotope systematics of Southern African peridotite xenoliths: implications for the chemical evolution of subcontinental mantle. Geochim. Cosmochim. Acta 53, 1583–1595.

Walker, R.J., Morgan, J.W., Horan, M.F., Czamanske, G.K., Krogstad, E.J., et al., 1994. Re–Os isotopic evidence for an enriched-mantle source for the Noril'sk-type, ore-bearing intrusions, Siberia. Geochim. Cosmochim. Acta 58, 4179–4197.

Walter, M.J., 1998. Melting of garnet peridotite and the origin of komatiite and depleted lithosphere. J. Petrol. 39 (1), 29–60.

Walter, M.J., 1999. Melting residues of fertile peridotite and the origin of cratonic lithosphere. In: Fei, Y., Bertka, C.M., Mysen, B.O. (Eds.), Mantle Petrology: Field Observation and High Pressure Experimentation. Spec. Publ. - Geochem. Soc., pp. 225–239.

Wass, S.Y., Hollis, J.D., 1983. Crustal growth in south-eastern Australia—evidence from lower crustal eclogitic and granulitic xenoliths. J. Metamorph. Geol. 1, 24–45.

Wasserburg, G.J., Jacobsen, S.B., DePaolo, D.J., McCulloch, M.T., Wen, T., 1981. Precise determination of Sm/Nd ratios, Sm and Nd isotopic abundances in standard solutions. Geochim. Cosmochim. Acta 45, 2311–2323.

Webb, S., Wood, B., 1986. Spinel–pyroxene–garnet relationships and their dependence on Cr/Al ratio. Contrib. Mineral. Petrol. 92, 471–480.

Wiechert, U., Ionov, D.A., Wedepohl, K.H., 1997. Spinel peridotite xenoliths from the Atsagin–Dush volcano, Dariganga lava plateau, Mongolia: a record of partial melting and cryptic metasomatism in the upper mantle. Contrib. Mineral. Petrol. 126, 345–364.

Witt-Eickschen, G., Seck, H., 1991. Solubility of Ca and Al in orthopyroxene from spinel peridotite: an improved version of an empirical geothermometer. Contrib. Mineral. Petrol. 106, 431439.

Witt-Eickschen, G., Kaminsky, W., Kramm, U., Harte, B., 1998. The nature of young vein metasomatism in the lithosphere of the west Eifel (Germany): geochemical and isotopic constraints from composite mantle xenoliths from the Meerfelder Maar. J. Petrol. 39 (1), 155–185.

Xu, X., O'Reilly, S.Y., Griffin, W.L., Zhou, X., 1999. Genesis of young lithospheric mantle in southeastern China: an LAM–ICPMS trace element study. J. Petrol. 41, 111–148.